Journal Pre-proof

Geochemistry, detrital zircon geochronology and Hf isotope of the clastic rocks in southern Tibet: implications for the Jurassic-Cretaceous tectonic evolution of the Lhasa terrane

Youqing Wei, Zhidan Zhao, Yaoling Niu, Di-Cheng Zhu, Donald J. DePaolo, Tianjing Jing, Dong Liu, Qi Guan, Lawangin Sheikh

PII: S1342-937X(19)30265-5

DOI: https://doi.org/10.1016/j.gr.2019.08.014

Reference: GR 2215

To appear in: *Gondwana Research*

Received Date: 30 May 2019

Revised Date: 20 August 2019

Accepted Date: 25 August 2019

Please cite this article as: Wei, Y., Zhao, Z., Niu, Y., Zhu, D.-C., DePaolo, D.J., Jing, T., Liu, D., Guan, Q., Sheikh, L., Geochemistry, detrital zircon geochronology and Hf isotope of the clastic rocks in southern Tibet: implications for the Jurassic-Cretaceous tectonic evolution of the Lhasa terrane, *Gondwana Research*, https://doi.org/10.1016/j.gr.2019.08.014.

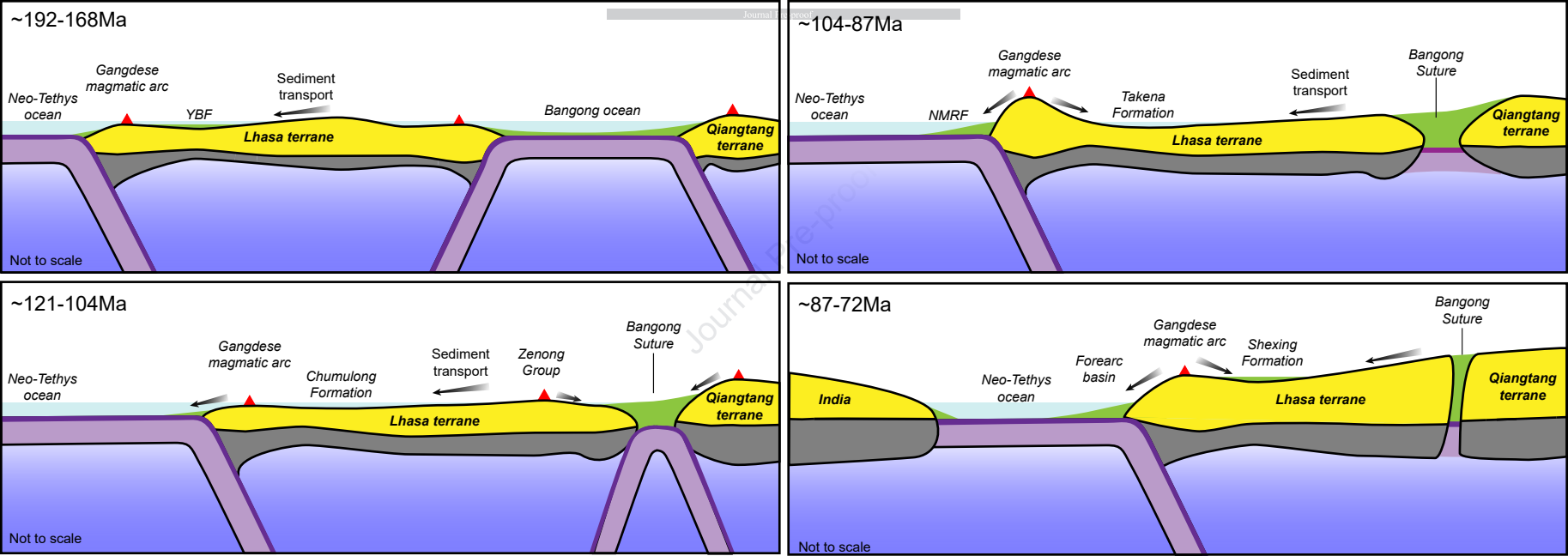
~192-168Ma
Neo-Tethys ocean
Gangdese magmatic arc
YBF
Sediment transport
Lhasa terrane
Bangong ocean
Qiangtang terrane
Not to scale
~104-87Ma
Neo-Tethys ocean
Gangdese magmatic arc
NMRF
Takena Formation
Sediment transport
Lhasa terrane
Bangong Suture
Qiangtang terrane
Not to scale
~121-104Ma
Neo-Tethys ocean
Gangdese magmatic arc
Chumulong Formation
Sediment transport
Zenong Group
Lhasa terrane
Bangong Suture
Qiangtang terrane
Not to scale
~87-72Ma
India
Neo-Tethys ocean
Forearc basin
Gangdese magmatic arc
Shexing Formation
Lhasa terrane
Bangong Suture
Qiangtang terrane
Not to scale

Geochemistry, detrital zircon geochronology and Hf isotope of the clastic rocks in southern Tibet: implications for the Jurassic-Cretaceous tectonic evolution of the Lhasa terrane

Youqing Wei[a,b,d], Zhidan Zhao[c,*], Yaoling Niu[a,c,d,e], Di-Cheng Zhu[c], Donald J. DePaolo[f], Tianjing Jing[c], Dong Liu[c], Qi Guan[g], and Lawangin Sheikh[c]

[a] Institute of Oceanology, Chinese Academy of Sciences, Qingdao 266071, China

[b] Shandong Provincial Key Laboratory of Depositional Mineralization & Sedimentary Mineral, Shandong University of Science and Technology

[c] State Key Laboratory of Geological Processes and Mineral Resources, and School of Earth Science and Resources, China University of Geosciences, Beijing 100083, China

[d] Laboratory for Marine Geology, Qingdao National Laboratory for Marine Science and Technology, Qingdao 266061, China

[e] Department of Earth Sciences, Durham University, Durham HD1 3LE, UK

[f] Department of Earth and Planetary Sciences, University of California, Berkeley, CA 94720

[g] Hebei GEO University, Shijiazhuang 050031, China

*Corresponding author at:

State Key Laboratory of Geological Processes and Mineral Resources, and School of

Earth Science and Resources, China University of Geosciences, Beijing 100083, China.

Tel: +86-10-82321115

E-mail: zdzhao@cugb.edu.cn

Abstract

In order to reconstruct tectonic evolution history of the southern margin of Asia (i.e., Lhasa terrane) before the India-Asia collision, here we present a comprehensive study on the clastic rocks in the southern Lhasa terrane with new perspectives from sedimentary geochemistry, detrital zircon geochronology and Hf isotope. Clasts from the Jurassic-Early Cretaceous sedimentary sequences (i.e., Yeba and Chumulong Formations) display high compositional maturity and experienced moderate to high degree of chemical weathering, whereas those from the late Early-Late Cretaceous sequences (Ngamring and Shexing Formations) are characterized by low compositional maturity with insignificant chemical weathering. Our results lead to a coherent scenario for the evolution history of the Lhasa terrane. During the Early-Middle Jurassic (~192-168Ma), the Lhasa terrane was speculated to be an isolated geological block. The Yeba Formation is best understood as being deposited in a back-arc basin induced by northward subduction of the Neo-Tethys ocean with sediments coming from the interiors of the Lhasa terrane. The Middle Jurassic-Early Cretaceous Lhasa-Qiangtang collision resulted in the formation of a composite foreland basin with southward-flowing rivers carrying clastic materials from the

uplifted northern Lhasa and/or Qiangtang terranes. During the late Early-Late Cretaceous (~104-72Ma), the Gangdese magmatic arc was uplifted rapidly above the sea level, forming turbidites (Ngamring Formation) in the Xigaze forearc basin and fluvial red beds (Shexing Formation) on the retro-arc side. At the end of Late Cretaceous, the Lhasa terrane was likely to have been uplifted to high elevation forming an Andean-type margin resembling the modern South America before the India-Asia collision.

Keyword: geochemistry; detrital zircon geochronology; Hf isotope; Lhasa terrane; southern Tibet

1 Introduction

The theory of plate tectonics explains the way how physiographic features of the Earth are shaped and evolve over time. Serving as an archetype of continent-continent collision, the Tibetan Plateau is thought to have influenced global climate and seawater chemistry (Molnar et al., 2010; Richter et al., 1992). It is widely accepted that the Tibetan Plateau is a Cenozoic feature resulting from the India-Asia collision and subsequent subduction of the Indian lithosphere beneath Asia (e.g., Chung et al., 1998; Harrison et al., 1992). However, recent investigations have proposed that the southernmost portion of Asia (i.e., the Lhasa terrane) might have attained high elevation immediately before the collision (Kapp et al., 2005, 2007; Leier et al., 2007a; Murphy et al., 1997; Zhu et al., 2017). It is crucial to ascertain the pre-collisional

tectonic evolution history of the Lhasa terrane for better understanding the mechanism and time-scale of the plateau formation.

Chemical composition holds important information on the provenance of clastic sedimentary rocks. Compared with petrographic method, the geochemical approach has been shown to be more effective in studying matrix-rich sandstones and shales, and in some cases can be used to quantify the occurrence and/or extent of sedimentary processes such as weathering, sorting and diagenesis (McLennan et al., 1993). Previous studies have correlated chemical weathering intensity of clastic rocks with climate and relief of the source terranes (e.g., Fedo et al., 1997; Nesbitt and Young, 1982; Yan et al., 2010). Sediments having undergone significant chemical weathering are likely to be deposited in low-relief regions with warm and humid climate (e.g., sediments of the Congo Rivers; Wronkiewicz and Condie, 1987), whereas those less affected by chemical weathering are supposed to be derived from high-relief regions with cold and arid climate (e.g., Pleistocene glacial clays and tillites; Nesbitt and Young, 1996). Existing paleomagnetic data show that the southern margin of the Lhasa terrane was close to the equator in the time span from the Early Jurassic (~3.7° S; Li et al., 2016) to Late Cretaceous (~15°N; Sun et al., 2012). In this case, climate change of the Lhasa terrane is largely related to tectonism-induced regional uplift, which can be best addressed using sedimentary geochemical approaches.

During chemical weathering, unstable components (including volcanic fragments, ferromagnesian minerals and feldspars) are largely decomposed but zircon survives

and is enriched in the sediments due to its physiochemical resistance. This makes zircon a powerful tracer for studying provenances of terrigenous sedimentary rocks (e.g., Wu et al., 2010; Zhu et al., 2011b). As potential provenance, the magmatic rocks emplaced in the southern Lhasa terrane and some localities in the northern Lhasa terrane have zircons with positive εHf(t), whereas rocks from the central Lhasa terrane have negative εHf(t) (Hou et al., 2015; Zhu et al., 2011a). Moreover, detrital zircons from the pre-Mesozoic rocks in the Lhasa terrane have a distinctive age cluster of ~1170Ma, whereas those from the western Qiangtang and Tethyan Himalaya terranes define an age peak of ~950Ma (Zhu et al., 2011b). The differences in detrital zircon age distribution and Hf isotopic composition serve as a unique tool for interpreting tectonic evolution history of the Lhasa terrane recorded in sedimentary rocks.

In this paper, we present the results of our study using a such combined approach, including bulk-rock geochemistry, detrital zircon U-Pb geochronology and Hf isotope on different types of clastic rocks (sandstones and mudstones) from the southern Lhasa terrane. Although previous studies have proposed numerous tectonic models for the Mesozoic Lhasa terrane based on magmatism (e.g., Hou et al., 2015; Zhu et al., 2011), tectonism (Yin and Harrison, 2000; Murphy et al., 1997) or stratigraphy (Kapp et al., 2005; Leier et al., 2007a), this paper is unique to provide new constraints on the changes of paleoclimate and sedimentary provenance through time. With these data, we are able to reconstruct the evolution history of the Lhasa terrane prior to the

India-Asia collision.

2 Geological background and sampling

2.1 Geological setting

The Tibetan Plateau comprises a series of allochthonous Gondwanan continental fragments that were accreted to Asia since the Early Paleozoic (Yin and Harrison, 2000; Zhu et al., 2013). These fragments are, from north to south, Songpan-Ganzi flysch complex, Qiangtang terrane, Lhasa terrane and the Himalayas, separated by Jinsha, Bangong and Indus-Yarlung Zangbo Sutures (Fig. 1A). Serving as the southernmost tectonic unit of Asia, the Lhasa terrane is an E-W trending geological block that can be divided into the northern, central and southern subterranes due to different magmatism and sedimentary covers (Hou et al., 2015; Zhu et al., 2011a). The ancient metamorphic basement of the Lhasa terrane is represented by the Nyainqentanglha Group in the central Lhasa terrane, which is covered with widespread Permian-Carboniferous metasedimentary strata (Zhu et al., 2011a, 2013). The northern Lhasa terrane has extensive Cretaceous strata and minor Triassic-Jurassic strata (Kapp et al., 2005, 2007; Zhu et al., 2011a). The southern margin of Lhasa terrane is represented by the Gangdese magmatic arc (GMA, Fig. 1A; also named as Gangdese batholith for the plutonic equivalents because of significant erosion), from which volcanism since the Middle Triassic has been well documented (e.g., Liu et al., 2018; Mo et al., 2008; Wang et al., 2016; Wei et al., 2017; Zhu et al.,

2008, 2011a). In the southern Lhasa terrane, sedimentary strata predominantly of Jurassic-Cretaceous age are well preserved (Zhu et al., 2013) and mainly comprise Lower-Middle Jurassic back-arc sequence of the Yeba Formation (Liu et al., 2018; Wei et al., 2017; Zhu et al., 2008) , Lower Cretaceous fluvial and marginal marine clastic successions of the Linbuzong and Chumulong Formations (Leier et al., 2007a), Upper Cretaceous shallow-marine deposits of the Takena Formation (Leier et al., 2007b) and fluvial red beds of the Shexing Formation (Sun et al., 2012) . There are also small-scale and scattered exposures of Upper Jurassic limestones of the Duodigou Formation showing fault contact with the underlying Yeba Formation. To the south of the Gangdese magmatic arc, a Cretaceous-Paleogene forearc succession was identified, i.e., Xigaze forearc basin (An et al., 2014; Wang et al., 2012; Wu et al., 2010). The Xigaze forearc succession is subdivided into the Chongdui, Sangzugang, Ngamring, Padana and Qubeiya Formations from the bottom to the top (Hu et al., 2016). Representing the main turbiditic fill of the Xigaze forearc basin, the Ngamring Formation displays conformable contact with underlying deep-water sediments of the Chongdui Formation and the overlying Padana Formation, and locally in fault contact with the Xigaze ophiolite in the south (An et al., 2014).

2.2 Sampling

2.2.1 Yeba Formation

Extending E-W trending for ~250km in the eastern segment of the southern Lhasa

144 subterrane, the Yeba Formation volcano-sedimentary strata comprise a bimodal
145 volcanic suite with interbedded fine-grained sandstone, calcic slate, and limestone
146 (Wei et al., 2017; Zhu et al., 2008). Two samples were collected from the fine-grained
147 sandstones exposed ~30km north of the Sangri County (Fig. 1B). These samples are
148 quartzose sandstone and are composed of subangular monocrystalline quartz, lithic
149 fragments and argillaceous cement with average modal composition of
150 Q/F/L=88/2/10 (Table S1; Fig. 3), where Q, F and L refer to quartz, feldspar and
151 lithics, respectively.

152 **2.2.2 Chumulong Formation**

153 Five mudstone samples were collected from the Chumulong Formation north of
154 Shannan city (Fig. 1B). The Chumulong Formation is dominated by dark-grey
155 mudstone with subordinate siltstone and sandstone. The mudstone is interbedded with
156 very fine-grained bioturbated sandstone with oyster fragments and fossil wood debris
157 (Fig. 2). This lithofacies association is interpreted as being deposited in a lagoon
158 environment (Leier et al., 2007a).

159 **2.2.3 Shexing Formation**

160 Eight sandstone samples were collected from the Shexing Formation red beds
161 (Fig. 2) northwest of Lhasa city (Figs. 1B). The sandstone units sampled are part of
162 a >2km-thick, strongly folded fluvial clastic succession which is covered by the

undeformed Paleogene Linzizong Group volcanic succession (LVS; Mo et al., 2008). These sandstones are feldspathic arenite and show large modal composition variations with average Q/F/L=35/27/38 (Table S1; Fig. 3).

2.2.4 Ngamring Formation

The flysch sequence of Ngamring Formation consists of alternating beds of sandstone and mudstone (Fig. 2) and is characterized by a series of large channelized conglomerates in the lower portion (Wang et al., 2012). Based on stratigraphy, sandstone petrography and detrital zircon age population, the Ngamring Formation can be further divided into three subsequences, i.e., the Lower, Middle and Upper Ngamring Formations (An et al., 2014; Wu et al., 2010). Eight samples were collected from the sandstone beds, among which RK1601, RK1602, RK1603 and RK1605 are from the Lower Ngamring Formation, RK1612 and RK1613 are from the Middle Ngamring Formation, and RK1614 and RK1615 are from the Upper Ngamring Formation. The samples are litharenite to feldspathic arenite and contain a large number of volcanic fragments (Table S1; Fig. 3) with average modal composition of Q/F/L=12/23/65.

3 Methods

Modal composition analysis was carried out on eighteen sandstone samples with 300 points counted per thin section using Gazzi-Dickinson method (Ingersoll et al.,

1984). The results are plotted in Fig. 3 and given in Table S1.

Detrital zircons were extracted from crushed samples using heavy liquid and magnetic separation techniques. Individual grains were handpicked, mounted in epoxy resins and then polished to expose the interiors. Zircon U-Pb ages were measured using LA-ICPMS at State Key Laboratory of Geological Processes and Mineral Resources (GPMR), China University of Geosciences, Wuhan, by following Liu et al. (2010a). Cathodoluminescence (CL) images were not referenced and all analyzed grains were selected randomly from all sizes and shapes during the analysis. The laser spot was 32 microns in diameter and always placed on the center of the zircon grain. Zircon standard 91500 was analyzed as external standard to correct for Pb isotope fractionation. Offline data calculations were processed using the program ICPMSDataCal_Ver8.0 (Liu et al., 2010b). The ages presented in this study are $^{206}Pb/^{238}U$ ages for zircons < 1000Ma and $^{207}Pb/^{206}Pb$ ages for those >1000Ma. The analyses with more than 20% discordance are omitted from further discussion. The kernel density estimation (KDE) plots were constructed using the software DensityPlotter (Vermeesch, 2012). Analyzed as an unknown, the zircon standard Plesovice yielded a mean $^{206}Pb/^{238}U$ age of 338±0.6Ma (2σ, n=117).

Maximum depositional age is determined using method of Dickinson and Gehrels (2009), who suggest both YSG (youngest single grain age) and YC1σ(2+) (weighted mean age of youngest detrital zircon cluster with two or more grains overlapping in age at 1σ) show similar compatibility with depositional age, but the former may be

suspicious due to inherent lack of reproducibility. The YC2σ(3+) (weighted mean age of youngest detrital zircon cluster with three or more grains overlapping in age at 2σ) is the most conservative measurement and considerably older than depositional age. Generally, YC1σ(2+) is preferred as maximum depositional age. In this study, the YSG is suggested for those whose YC1σ(2+) are inconsistent with the depositional ages determined via other samples/methods. Detrital zircon U-Pb data are summarized in Table 1 and plotted in Fig. 4.

In-situ zircon Hf isotope analysis was conducted using LA-MC-ICPMS in the Institute of Geology and Geophysics, Chinese Academy of Sciences (IGGCAS). Zircon grains were ablated using a 193nm excimer ArF laser (GeoLas Plus) with a spot diameter of 45-60 microns. Ablated material was carried by helium and introduced into a Neptune MC-ICPMS. The analytical details were given by Wu et al. (2006). The U-Pb dating and Hf isotope raw data are present in Tables S2 and S3.

Whole rock major and trace element analyses were carried out at GPMR, Wuhan. Major element oxide measurement was done using a SHIMADZU sequential X-ray fluorescence spectrometer (XRF-1800) following Ma et al. (2012). The analytical uncertainties are better than 3%. Trace elements were determined using an Agilent 7500a ICP-MS by following Liu et al. (2008). The analytical results are presented in the Table S4.

4 Results

4.1 Detrital zircon geochronology and Hf isotope

4.1.1 Yeba Formation

A total of 104 usable detrital zircon ages show a large variation from 179±2 to 3520±20Ma (Figs. 4A, 4B). Pre-Mesozoic ages comprise the largest population (99 out of 104 results), which form significant peaks centered at 556 and 1170Ma. The depositional interval age has been yielded to Early-Middle Jurassic (~168-192Ma) via zircon geochronologic study on the volcanic sequences within the Yeba Formation strata (Liu et al., 2018; Wei et al., 2017; Zhu et al., 2008). Therefore, although the YC1σ(2+) and YC2σ(3+) of sample D54 was yielded to 563.5±3.6 and 248.0±3.5Ma, respectively, the maximum depositional age is supposed to be 179Ma using the youngest single zircon grain age (YSG).

4.1.2 Chumulong Formation

The four Chumulong samples yield 327 usable ages (Figs. 4C, 4D). Sample D47A yields 103 usable ages ranging from 117±1 to 2595±14Ma with major peaks at 121 and 224Ma. Sample D47B yields 109 usable ages ranging from 105±1 to 2732±29Ma, which form four peaks at 123, 143, 166 and 226Ma. Only 47 usable ages are obtained from sample D47E, among which the largest population peaks at 231Ma. Among the 68 available analyses for the sample D47C, zircons with Paleozoic ages are predominant

(63 out of 68 results) with significant age peaks at 404 and 454Ma. The maximum depositional age for the Chumulong Formation is recommended to be 121Ma using the YC1σ(2+) of sample D47A.

In-situ Hf isotope analysis was performed on 208 zircon grains that had not been exhausted after the U-Pb age analysis. Zircon grains with Mesozoic ages display a large variation in $^{176}Hf/^{177}Hf$ ratios with εHf(t) ranging from -24.3 to +14.7, revealing the source rock diversity (Fig. 5).

4.1.3 Shexing Formation

The four Shexing samples yield 377 usable ages (Figs. 4E, 4F). Sample MX1102 yields 113 usable ages with the youngest being 84±2 Ma. This sample contains a large population of pre-Mesozoic zircons peaking at 550, 700, 1450, 1750 and 2600Ma, whereas Mesozoic ages are subordinate (28 out of 113 results) with peaks at 88 and 121Ma. Sample MX1104 yields 90 usable ages that exhibit a major peak at 90Ma and a subordinate at 112Ma. Sample MX1106 yields 86 usable ages with the youngest being 82±2Ma. Mesozoic zircons are predominant (71 out of 86 spots) showing a major peak at 88Ma and a subordinate at 201Ma. Sample MX1108 yields 88 usable ages, most of which are pre-Mesozoic (82 out of 88 spots). Only four grains are identified with Cretaceous ages of 91±2Ma, 92±2Ma, 105±4Ma and 121±5Ma. This sample yielded numerous small clusters and scatters showing no significant peaks. The maximum depositional age for the Shexing Formation is supposed to be 88Ma using the YC1σ(2+)

of sample MX1106.

Mesozoic zircons from these samples exhibit varying Hf isotope composition (Fig. 5). Zircons with ages <105Ma have high $^{176}Hf/^{177}Hf$ ratios with $\varepsilon_{Hf}(t)$ ranging from -0.6 to +13.7, whereas those with ages between 109 and 238Ma show varying $^{176}/Hf/^{177}Hf$ with $\varepsilon_{Hf}(t)$ ranging from -16.1 to +5.4.

4.2 Bulk-rock geochemistry

4.2.1 Major elements

The Yeba and Chumulong samples as a whole display higher compositional maturity than those of the Ngamring and Shexing Formations. In terms of major oxides, the Yeba sandstones are potassic (K_2O/Na_2O=5.64-7.04) with higher SiO_2, lower Al_2O_3, and Na_2O (Figs. 6B, 6D and 6F). The Chumulong mudstones have similar SiO_2 (63.82±5.90wt.%) but higher Al_2O_3 (19.06±2.26wt.%) relative to the average composition of the upper continental crust (SiO_2~66.3wt.%, Al_2O_3~14.9wt.%; Rudnick and Gao, 2003). Compared with those of the Yeba Formation, the Shexing sandstones are typically sodic (K_2O/Na_2O=0.16-0.57, except for sample MX1103 ~1.14) and have a wider range of SiO_2, Al_2O_3 and CaO abundances (Figs. 6B and 6E). Similarly, the Ngamring samples display sodic characteristics (K_2O/Na_2O=0.12-0.58) with relatively low SiO_2 (55.9±13.4wt.%). The high LOI values of the Ngamring samples (4.37-10.29 wt.%) are attributed to the presence of detrital carbonate in terms of petrographic observation and the positive CaO-LOI correlation (r=0.97). Generally,

in the sandstones, there are marked negative correlations of SiO_2 with TiO_2, Al_2O_3, $MgO+Fe_2O_3^T$ (where $Fe_2O_3^T$ represents total Fe as Fe_2O_3) and Na_2O (Figs. 6A, 6B, 6C, 6E and 6F), reflecting increasing compositional maturity towards high SiO_2. It is noted that Mg, Fe, Ti and Na largely reside in the volcanic lithic fragments, reflected by the negative correlation of modal volcanic lithics proportion with these elements (Figs. 6G, 6H and 6I).

4.2.2 Trace elements

All the samples have subparallel REE patterns (Fig. 7). The Yeba and Chumulong samples show smoothly fractionated patterns with La/Yb_N of 7.23 – 15.2 (where subscript *N* refers to chondrite-normalized values) and Eu/Eu* of 0.55 – 0.72. The former has lower ΣREE (refers to total REE) abundances (99±28 ppm) than the latter (180±30 ppm) due to quartz dilution effect. The Shexing samples have similar REE distributions (La/Yb_N=8.09-10.2) but weak or absent Eu anomalies (Eu/Eu*=0.63-1.00) with lower ΣREE abundances (125±44 ppm). The Ngamring samples are characterized by relatively flat patterns with lowest La/Yb_N ratios (4.10-8.39), ΣREE abundances (74±21 ppm) and Eu/Eu* ranging from 0.77 to 1.05. In the sandstone samples, Eu/Eu* is most likely controlled by the enrichment of plagioclase-rich volcanic lithic fragments (Fig. 6L). This suggests that these samples were deposited in a volcanically active region with short transport distance of the clastics.

In the upper continental crust normalized multielement diagram (Fig. 7E), patterns of the Shexing and Ngamring samples are subparallel to the unweathered Yeba volcanic rocks (except for individual element), which are concordant with predominant magmatic provenances. The Yeba and Chumulong samples show gradually reduced depletion in the order of Na, Sr, Ba and K. Rb is enriched in the Chumulong mudstones probably due to the adsorption by clays. The transition metals (Co, Ni, Cr, and V) are largely inherited from the volcanic lithic fragments (Fig. 6J) in the sandstone samples. Th and U are generally coherent during most magmatic processes; however, they may be fractionated during weathering and sedimentary recycling processes. The Ngamring, Shexing, Yeba and Chumulong samples have gradually increasing Th/U ratios of 3.14±1.47, 4.66±1.09, 4.91±0.31 and 6.04±0.76, respectively. See below for detailed discussion.

5 Influence of sedimentary processes on elemental variations

Chemical composition of terrigenous sedimentary rocks is the net result of various factors, which includes provenance, weathering, sorting, diagenesis and post-depositional metamorphism. Each of these processes should be taken into account when speculating tectonic implications using geochemical data. It is suggested that the Yeba Formation has undergone up to greenschist-facies metamorphism (Wei et al., 2017; Zhu et al., 2008). In this case, the unweathered Yeba Formation volcanic rocks with greenschist-facies metamorphism are introduced into

the next discussion for estimating the influence of metamorphism on the compositional variation of the clastic rock samples.

5.1 Weathering and diagenesis

Chemical weathering modifies the composition of rocks via water-rock interaction. With increasing intensity of chemical weathering, there is typically an increase in clays at the expense of unstable components such as volcanic lithic fragments, ferromagnesian minerals and feldspars. Meanwhile, the soluble alkali or alkaline-earth metals (AAEM) with smaller ironic radius tends to be preferentially leached from the soils than the larger one that is more readily retained on exchange sites of clay minerals (McLennan et al., 1993). The Yeba and Chumulong clastic samples show an increasing depletion tendency towards the smaller AAEM cations (Fig. 7E), indicating that their precursors were subjected to significant chemical weathering. Compared with the clastic rock samples, the Yeba volcanic rocks show a distinct AAEM pattern with high Na and Sr abundances, suggesting the regional metamorphism has played no dominant role in modifying the AAEM composition of the Yeba Formation. In contrast, the AAEM patterns of the Shexing and Ngamring clastic samples are similar to that of the Yeba Formation volcanic rocks (Fig. 7E), revealing that the source rock disaggregation was primarily controlled by physical weathering with restricted chemical modification.

To better quantify the degree of chemical weathering, Chemical Index of

341 Alteration (CIA) is used here (Nesbitt and Young, 1982): CIA=Al_2O_3/[Al_2O_3 + K_2O +
342 Na_2O + CaO*]×100, where CaO* refers to that residing in silicate minerals only. In
343 this case, a correction should be made through subtracting the CaO from carbonate
344 and apatite. In this study, the CaO is preferentially corrected for apatite using
345 bulk-rock P_2O_5 abundance (mole CaO_{corr} = mole CaO – mole P_2O_5 ×10/3). If the
346 mole CaO_{corr} is less than Na_2O, its value is adopted as the CaO*; otherwise the CaO*
347 value is assumed to be equivalent to Na_2O (McLennan et al., 1993; Yan et al., 2010).
348 The CIA value is directly related to chemical weathering intensity, from 50 in
349 unweathered igneous rocks to 100 in residual clays. According to the existing data
350 (Wei et al., 2017), the Yeba volcanic rocks with greenschist-facies metamorphism
351 have a mean CIA value of ~50, confirming that the post-depositional metamorphism
352 had not significantly increased the CIA values of the Yeba Formation rocks. For better
353 visualizing the significance of CIA values, the samples are plotted on the A-CN-K
354 ternary diagram (Fig. 8A). The Yeba and Chumulong samples show moderate to high
355 degree of chemical weathering with CIA values ranging from 71 to 81, which are
356 significantly higher than the Yeba volcanic rocks but similar to that of the typical
357 shale (~70-75; Taylor and McLennan, 1985). The Shexing and Ngamring samples
358 have lower CIA values of 49 to 59, revealing limited chemical modification and short
359 distance transportation of the clastics. All the samples fall on a trend deviating from
360 that of diagenetic K-metasomatism (smectite-illite transformation; Fedo et al., 1995),
361 but consistent with weathering being the sole control (McLennan et al., 1993). When

plotted in A-CNK-FM ternary diagram (Fig. 8B), the samples show trends that are best understood as mixing sources. These results further indicate that the CIA values of the clastic samples were decoupled from the compositional variation of their precursors.

Another geochemical index, Th/U, is commonly used to estimate the impact of chemical weathering (McLennan et al., 1993; Taylor and McLennan, 1985). In most cases, chemical weathering under oxidizing environment can transform U^{4+} to more soluble U^{6+}. The subsequent dissolution and loss of U^{6+} results in elevation of Th/U in clastic rocks, especially for mudstones and shales, where heavy minerals are less likely to be an interfering factor (McLennan et al., 1993). It appears that the data follow the trend consistent with weathering being the primary control (Fig. 9); however, the Yeba samples show indistinguishable Th/U ratios and Th abundances from the Shexing counterparts, which contradict their distinct CIA values. It is also noted that the Th/U ratios in the sandstone samples overlap with those of the Yeba volcanic rocks (Fig. 5C) and are proportional to the content of volcanic lithics (Fig. 3K). Therefore, we suggest that Th/U ratios of the sandstones largely reflect the nature of the provenance rocks rather than the extent of chemical weathering.

5.2 Hydraulic sorting

The most commonly used approach to examine the influence of sorting on sedimentary rocks is to evaluate the textural maturity using characteristic grain sizes

and shapes (McLennan et al., 1993). Sorting processes are usually accompanied by fractionation or enrichment of heavy minerals (notably zircon), which can significantly modify abundances of the elements that are at trace levels in most sedimentary rocks (e.g., Zr and Hf in zircon). Therefore, geochemical composition of clastic rocks is also useful in evaluating the impact of sorting. Zr/Sc ratio is a promising tracer for zircon accumulation, since Zr is mostly concentrated in zircon whereas Sc is not enriched but generally inherited from the precursors. Th/Sc ratio is suggested as a potential indicator of magmatic differentiation, because Th behaves conservative during sedimentary processes (McLennan et al., 1993). In most of the samples, Zr/Sc covaries with Th/Sc, which can be attributed to compositional variation of the precursors. Note that the Chumulong samples show some variation in Zr/Sc with unvarying Th/Sc (Fig. 10A). Generally, fine-grained clastic rocks such as shales and mudstones are deposited in low-energy environment so that they are less prone to accumulating zircon. In this case, the Zr/Sc variations in the Chumulong samples are best understood as a consequence of hydraulic sorting. Considering that zircon is a weathering-resistant mineral with high density, its fractionation during sedimentary processes reveals a long-distance transportation of the clastic materials before deposition. The other sandstone samples lie on the trend that is consistent with compositional variations of the source rocks, indicating insignificant zircon fractionation. In some sediments of mineralogical immaturity, sorting can result in accumulation of plagioclase and volcanic fragments (McLennan et al., 1993). In the

Ngamring and Shexing sandstones, the Eu/Eu* is most likely controlled by the enrichment of plagioclase-rich volcanic lithic fragments (Fig. 3L), suggesting that the samples were deposited in a volcanically active region with short distance transportation of the clastic materials.

5.3 Two-component mixing model

Elements having conservative behavior in sedimentary processes and low residence time in seawater, such as Th, Nb, Zr, Co, Sc and LREEs, are promising indicators for the source rock signature (Bhatia and Crook, 1986). In the Th-Sc-Zr/10 ternary diagram (Fig. 10A), most of the samples show compositional similarity to the clastic rocks from oceanic or continental arcs. The Chumulong samples show a linear trend away from the Zr/10 apex, consistent with the fact that mudstones are depleted in zircon due to sorting. In the Fig. 10B, the samples plotted in the array of Gangdese magmatic arc, likely signifying mixing of two endmembers (mafic and silicic source rocks). A diagram of La/Sc vs. Co/Th (Fig. 11) is constructed to further test the two-component mixing model. All the data points lie on the mixing curve and show good agreement with the bimodal mixing model. The Ngamring samples display largest compositional variations, among which RK1605 with lowest SiO_2 abundance (46.7 wt.%) and highest Co/Th ratio (21.2) requires >90% mafic component contribution. This result is concordant with the petrographic observation showing a large proportion of basaltic lithic fragments in the Ngamring samples, and reveals that

the low SiO_2 abundances of the Ngamring samples are not attributed to the presence of carbonate characterized by low Co/Th ratio. The Shexing samples have overall intermediate to silicic provenance with >50% silicic component contribution. The Yeba and Chumulong sediments have most acidic provenance with >80% silicic component.

6 Sedimentary provenances and tectonic implication

6.1 Yeba Formation (~192-168Ma)

The Yeba sandstones are characterized by high CIA values and significant negative Eu/Eu* anomalies (Fig. 7) with strong depletion in alkali and alkaline earth metals (Fig. 7E), indicating a low-relief provenance with tropical climate. According to the mixing model (Fig. 11), the Yeba sandstones are best interpreted as being sourced from silicic provenance. Petrographic observation shows that the modal compositions of the Yeba samples fall into the recycled orogen region in the Q-F-L plot (Fig. 3). Detrital zircon data reveal that the Yeba Formation sediments were recycled from the pre-Jurassic strata in the Lhasa terrane without exotic clastic addition, because: (1) the Mesozoic ages are relatively rare (~5.7%, 6 out of 104 results) in the sample D54, suggesting a limited supply of juvenile materials; and (2) the age spectrum is subparallel to those of the Paleozoic and Triassic metasedimentary rocks (notable age peak of ~1170Ma; Figs. 13B, 13C, 13D) in the Lhasa terrane but distinct from those of the western Qiangtang clastic rocks (characterized by significant peak

443 of ~950Ma; Fig. 13G). These results suggest that the Lhasa terrane was an isolated
444 geological block drifting in the Tethyan ocean and had not collided with the
445 Qiangtang terrane during the Early Jurassic.

446 Previous research has suggested that subduction zones were developed on both
447 northern and southern sides of the Lhasa terrane (Zhu et al., 2013; 2016). Substantial
448 Triassic-Jurassic subduction-related volcanism (237-168Ma) occurred in the southern
449 Lhasa subterrane (e.g., Kang et al., 2014; Liu et al., 2018; Tafti et al., 2014; Wang et
450 al., 2016; Wei et al., 2017) indicates that the northward subduction of the
451 Neo-Tethyan oceanic lithosphere beneath the Lhasa terrane should initiate prior to the
452 Middle Triassic (Wang et al., 2016). An alternative view presumed that the Early
453 Mesozoic magmatism was induced by southward subduction and rollback of the
454 Bangong Tethyan oceanic lithosphere (Zhu et al., 2013). It is noted that the
455 Triassic-Jurassic subduction-related volcanism exposed in the area ~250-300km south
456 of the Bangong Suture without considering ~60% crustal shortening occurring during
457 the Late Jurassic – Cretaceous (Murphy et al., 1997). However, the mean distance
458 from arc volcanoes to trench in the modern subduction zones is 166±60km (Stern,
459 2002). In this case, it is more reasonable that the volcanisms in southern Lhasa terrane
460 were associated with northward subduction of the Neo-Tethyan oceanic lithosphere.

461 In the southern Lhasa terrane, the subduction-related Xiongcun porphyry Cu
462 deposit with ore-bearing country rocks of the Early-Middle Jurassic Xiongcun
463 Formation volcano-sedimentary sequence was developed to the west of the Yeba

Formation (Lang et al., 2014, 2018; Tafti et al., 2009; 2014; Tang et al., 2015). Sillitoe (1998) favored the compressional regime for the formation of subduction-related porphyry Cu deposits in terms of the statistic study on global Cu deposits; however, no Cu deposits have been found in the Yeba Formation, which was previously considered to be formed in continental arc setting (Zhu et al., 2008). The Xiongcun sandstones are classified as lithic arenite and have modal composition of Q/F/L=21:11:68 (Fig. 3) with positive detrital zircon Hf isotopic fingerprints (+10.5 to +16.2) (Lang et al., 2018). These results indicate that the Xiongcun and Yeba sandstones were deposited in different tectonic settings. The high proportion of volcanic lithic fragments reveals that the Xiongcun sandstones were sourced from uplifting volcanic arcs, while the high degree of chemical weathering (CIA =77-85) suggests a tropical climate (Lang et al., 2018). The Yeba sandstones, however, are predominated by recycled quartz and underwent high chemical weathering, indicating that they were gradually deposited in the basin with relatively subdued uplift and low elevations (Fig. 14A). A reasonable explanation is that the Yeba Formation was deposited in the back-arc basin close to the central Lhasa terrane, whereas the Xiongcun Formation represents the Gangdese volcanic arc front. The southern margin of the Lhasa terrane most likely resembles the present-day Ryukyu-Okinawa arc-basin system in the Early-Middle Jurassic. This proposal is reinforced by the study on the volcanic rocks suggesting the Yeba Formation were formed in extensional setting (Liu et al., 2018; Wei et al., 2017).

6.2 Chumulong Formation (~121-105Ma)

In this study we calculate a maximum depositional age of 121Ma for the Chumulong Formation, which is ~22Myrs younger than reported in Leier et al. (2007c). The Chumulong samples have similar geochemical characteristics to the Yeba Formation counterparts (i.e., high CIA values, low Na_2O/K_2O, strong depletion in Na^+ and Sr^{2+} and significant negative Eu anomalies; Figs. 7E and 12), revealing a high degree of chemical modification during weathering and clastic transportation processes. Taking into account that the Chumulong Formation is dominated by mudstones and subordinate fine-grained sandstones accompanied with fossil wood debris, we suggest that the climate and relief were not markedly changed from the Jurassic and the southern Lhasa terrane maintained at low elevations (Fig. 13C).

Note that detrital zircon data indicate that source regions of the Early Cretaceous sediments were inconsistent with the pre-Cretaceous samples. Firstly, detrital zircon age peak of ~950Ma appears in the Early Cretaceous samples (Fig. 12E). Secondly, the Early Cretaceous samples show insignificant age population around ~1170Ma, which differs from those of the pre-Cretaceous samples. These results strongly imply a Middle-Late Jurassic tectonic event that could result in the change of source region of the sediments in the Lhasa terrane. One of the most significant tectonic events for the Lhasa terrane prior to the India-Asia collision is its collision with the Qiangtang terrane, which was speculated to initiate as early as the Middle Jurassic (Lai et al., 2019; Li et al., 2019; Sun et al., 2019) and completed during the Late Jurassic to Early

506 Cretaceous (Zhu et al., 2016). The discrepancies of detrital zircon age spectra between
507 the pre-Cretaceous and Cretaceous samples are best interpreted as resulting from the
508 Lhasa-Qiangtang collision. As a consequence, a foreland basin was probably formed
509 in the Lhasa terrane (Figs. 13B) and clasts from Qiangtang were transported to the
510 Lhasa terrane by south-directed rivers. This proposal is supported by the appearance
511 of the Berriasian-Valanginian (~145-134Ma) foreland molasse association in the
512 central Lhasa terrane with paleocurrent directions mainly toward the south (Zhang et
513 al., 2012).

514 However, a simple foreland basin model is probably insufficient to explain the
515 sedimentary records in the northern Lhasa terrane. During the Early Cretaceous,
516 extensive volcanism (i.e., Zenong Group; Zhu et al., 2011a) occurred in the northern
517 Lhasa terrane and overprinted the foreland basin in some localities. Subordinate
518 basins (e.g., Coqen and Selin Co basins; Sun et al., 2017; Zhang et al., 2011) were
519 consequently formed with deposition of the Duoni Formation. Sun et al. (2017)
520 suggested that the Duoni Formation was mainly sourced from the Zenong volcanic
521 rocks and basement rocks from the southern portion of the northern Lhasa subterrane.
522 It is also noted that the detrital zircons from the Duoni clastic rocks exhibit significant
523 age peaks of 950 and 1170Ma (Leier et al., 2007c; Zhang et al., 2011), similar to those
524 of the Early Cretaceous samples in the southern Lhasa terrane (Fig. 12E). Furthermore,
525 the detrital zircons are characterized by negative εHf(t) (Fig. 5), implying no sediment
526 supply from the Gangdese magmatic arc to the south. Paleocurrents measured from

Duba section of the Duoni Formation and Linzhou section of the Chumulong Formation are overall south-directed, although few of them indicate north-directed flows (Leier et al., 2007a). Considering all the geological evidences, we suggest that clastic contribution from the Qiangtang terrane cannot be precluded in the Early Cretaceous sedimentary basins of the northern Lhasa terrane, and the Lhasa terrane was still a south-dipping foreland basin as a whole. This model is consistent with the study of Wang et al., (2017b) on Damxung conglomerates in the central Lhasa terrane, who suggested the initial topographic growth took place in the northern part of the Lhasa terrane by the early Albian time. A composite foreland basin model (Fig. 14C) is suitable, where multiple subordinate sedimentary basins were developed with clastic materials coming from both the Qiangtang terrane and the interiors of the Lhasa terrane.

6.3 Ngamring Formation (~104-83Ma)

As the first and main turbiditic fill of the Xigaze forearc basin (An et al., 2014; Wang et al., 2012), the Ngamring Formation is in conformable contact with underlying deep-water sediments of the Chongdui Formation (Wang et al., 2017a). The change of lithofacies association from deep-water sediments to turbidites indicate a late Early Cretaceous tectonic event occurred along the southern margin of the Lhasa terrane. Overall, the Ngamring sandstones are characterized by low CIA values, high Na_2O/K_2O and weak to absence of Eu anomalies, displaying high compositional

547 and textural immaturity (Fig. 12). The Lower Ngamring Formation is supposed to
548 have a maximum depositional age of 104Ma (An et al., 2014). The Lower Ngamring
549 samples are characterized by low SiO_2 and high Na_2O/K_2O, from which detrital
550 zircons are predominately of Cretaceous age with positive εHf(t) values (An et al.,
551 2014; Wu et al., 2010). According to the two-component mixing model (Fig. 11),
552 significant contribution of mafic component (40-92%) is required for the Ngamring
553 sandstones. These results reveal that the Gangdese magmatic arc was in a period of
554 strong volcanic activities, consistent with the petrographic observation showing
555 abundant volcanic lithic fragments in the Ngamring samples. Therefore, we advocate
556 that the Gangdese magmatic arc was quickly uplifting above sea level (Fig. 14D) and
557 changing the shelf and submarine canyon morphology since the late Early Cretaceous.
558 Leier et al. (2007b) drew a similar conclusion via addressing the sandstone
559 provenance of the age-equivalent Takena Formation in the north of the Gangdese
560 magmatic arc. Samples of the Middle Ngamring Formation (~99-88Ma; An et al.,
561 2014) have higher SiO_2 and lower Na_2O/K_2O than the Lower Ngamring counterparts
562 indicating an additional supply of dissected magmatic arc materials. This inference
563 can be verified by the appearance of older detrital zircons peaking at ~157Ma with
564 positive εHf(t) values in the Middle Ngamring sandstones (An et al., 2014; Wu et al.,
565 2010). This means that by this time the south-flowing rivers had penetrated the
566 Gangdese magmatic arc. Samples of the Upper Ngamring Formation (~88-84Ma; An
567 et al., 2014; Wu et al., 2010) are the most acidic with lowest Na_2O/K_2O, showing

diversity of the source rocks. Abundant pre-Cretaceous detrital zircons with large variation of εHf(t) values in the Upper Ngamring sandstones suggest the sediments be transported from the northern portion of the Lhasa terrane or even from the Qiangtang terrane. The expansion of river catchments was most likely to be the result of regional uplift of the northern Lhasa and Qiangtang terranes during the Late Cretaceous. Above all, the Ngamring Formation turbidites record the denudation of the Gangdese magmatic arc, which reflects uplifting history of the southern margin of the Lhasa terrane.

6.4 Shexing Formation (~87-72Ma)

It is suggested that deposition of the Shexing Formation likely initiated by ~87Ma constrained by detrital zircon geochronology in this study, and ended by ~72Ma yielded by the volcanic rocks interbedded in the uppermost Shexing sequence (Sun et al., 2012). Characterized by low CIA, K_2O/Na_2O, weak to absence of Eu anomalies and large proportion of lithic grains, the Shexing sandstone samples illustrate a tectonically active source region that was rapidly uplifting with surface rocks disintegrated by physical weathering. Consider that the Lhasa terrane located at low latitudes (~15°N) during the Late Cretaceous, a high altitude (cold climate) is required to keep the chemical weathering intensity of the Shexing sandstones to a low level. A counter example is the Xiongcun lithic arenite with high chemical weathering intensity, which indicates the Lhasa terrane was at low elevation during the Jurassic. A

possible mechanism for the Late Cretaceous uplift of the Gangdese magmatic arc is the Neo-Tethyan mid-ocean ridge subduction (Zhang et al., 2010). The positive εHf(t) values of young detrital zircons (<105Ma) indicate that the Gangdese magmatic arc serves as a main provenance. This inference is further supported by the paleocurrents recording locally northward-flowing rivers during the Late Cretaceous (Leier et al., 2007b). Considering that there are also abundant Mesozoic detrital zircons with εHf(t)<0 (Fig. 5), more sources in addition to the Gangdese magmatic arc are required for the Shexing sandstones. Detrital zircon age spectrum of the Late Cretaceous samples (Fig. 13F) shows more evident peaks of ~800Ma and ~950Ma than the Early Cretaceous samples, revealing an increasing sediment supply from the Qiangtang terrane during the Late Cretaceous.

These results reconcile that the Lhasa and Qiangtang terranes were uplifted simultaneously during the Late Cretaceous (Fig. 14E). At the end of the Cretaceous, the crust of the Lhasa terrane was likely thickened to approximately twice the normal thickness prior to the India-Asia collision (Kapp et al., 2005, 2007; Murphy et al., 1997; Zhu et al., 2017).

7 Summary

(1) Twenty-Three Jurassic-Cretaceous clastic rock samples from the southern Lhasa terrane were analyzed for petrology and major and trace elements composition with the aim of illustrating the possible tectonic evolution of the Lhasa terrane.

Overall, the samples from the Yeba and Chumulong Formations show higher compositional maturity than those of the Ngamring and Shexing Formations. All the samples display smooth REE patterns with LREE enrichment and varying Eu anomalies.

(2) Sediments from the Jurassic-Early Cretaceous sequences (i.e., Yeba and Chumulong Formations) show high textural and compositional maturity and experienced moderate to high degree of chemical weathering, whereas those from the Late Cretaceous sequences (i.e., Ngamring and Shexing Formations) are characterized by low textural and compositional maturity and less affected by chemical weathering.

(3) Maximum depositional ages of the strata in the southern Lhasa terrane are estimated to be 179Ma for the Yeba Formation, 121Ma for the Chumulong Formation and 87Ma for the Shexing Formation. In-situ Hf isotope data show either positive or negative εHf(t) for the detrital zircons with Mesozoic ages, revealing a joint contribution of juvenile (from the Gangdese magmatic arc) and recycled (from the Qiangtang terrane and the interiors of the Lhasa terrane) components to the Cretaceous sediments in the southern Lhasa terrane.

(4) During the Early-Middle Jurassic (~192-168Ma), arc-basin system was developed in the southern Lhasa terrane. The Middle Jurassic-Early Cretaceous Lhasa-Qiangtang collision has resulted in the formation of a composite foreland basin with southward-flowing rivers carrying clastic materials from the uplifted northern Lhasa and/or Qiangtang terranes.

(5) From the late Early Cretaceous to Late Cretaceous (~104-72Ma), the Gangdese magmatic arc was uplifted rapidly above the sea level, forming turbidites (Ngamring Formation) in the Xigaze forearc basin and fluvial red beds (Shexing Formation) on the retro-arc side. At the end of the Late Cretaceous, the entire Lhasa terrane was likely to have been uplifted to high elevations forming an Andean-type margin in the south before the India-Asia collision.

Acknowledgements

This study was financially supported by grants from the National Key R & D Project of China (2016YFC0600304), the Natural Science Foundation of China (41806080, 41602040), Shandong Provincial Key Laboratory of Depositional Mineralization & Sedimentary Mineral (DMSM2018059), the Fundamental Research Funds for the Central Universities (2652018122) and 111 project (B18048, B07011). We are grateful for careful reviews by two anonymous reviewers, which greatly helped us improve the paper. Editor M. Santosh was thanked for editorial handling.

References

An, W., Hu, X., Garzanti, E., Boudagher-Fadel, M.K., Wang, J., Sun, G., 2014. Xigaze forearc basin revisited (South Tibet): Provenance changes and origin of the Xigaze Ophiolite. Geological Society of America Bulletin 126, 1595-1613.

Bhatia, M.R., Crook, K.A.W., 1986. Trace element characteristics of graywackes and

tectonic setting discrimination of sedimentary basins. Contribution to Mineralogy and Petrology 92, 181-193.

Cai, F., Ding, L., Laskowski, A.K., Kapp, P., Wang, H., Xu, Q., Zhang, L., 2016. Late Triassic paleogeographic reconstruction along the Neo–Tethyan Ocean margins, southern Tibet. Earth and Planetary Science Letters 435, 105-114.

Chung, S.-L., Lo, C.-H., Lee, T.-Y., Zhang, Y., Xie, Y., Li, X., Wang, K.-L., Wang, P.-L., 1998. Diachronous uplift of the Tibetan plateau starting 40 Myr ago. Nature 394, 769.

Cohen, K.M., Finney, S.C., Gibbard, P.L., Fan, J.-X., 2013. The ICS International Chronostratigraphic Chart. Episodes 36, 199-204.

Dickinson, W.R., 1985. Interpreting Provenance Relations from Detrital Modes of Sandstones, in: Zuffa, G.G. (Ed.), Provenance of Arenites. Springer Netherlands, Dordrecht, pp. 333-361.

Dickinson, W.R., Gehrels, G.E., 2009. Use of U–Pb ages of detrital zircons to infer maximum depositional ages of strata: A test against a Colorado Plateau Mesozoic database. Earth and Planetary Science Letters 288, 115-125.

Fedo, C.M., Wayne Nesbitt, H., Young, G.M., 1995. Unraveling the effects of potassium metasomatism in sedimentary rocks and paleosols, with implications for paleoweathering conditions and provenance. Geology 23, 921-924.

Fedo, C.M., Young, G.M., Nesbitt, H.W., 1997. Paleoclimatic control on the composition of the Paleoproterozoic Serpent Formation, Huronian Supergroup,

669 Canada: a greenhouse to icehouse transition. Precambrian Research 86, 201-223.

670 Harrison, T.M., Copeland, P., Kidd, W.S.F., Yin, A., 1992. Raising Tibet. Science 255,

671 1663-1670.

672 Hou, Z., Duan, L., Lu, Y., Zheng, Y., Zhu, D., Yang, Z., Yang, Z., Wang, B., Pei, Y.,

673 Zhao, Z., 2015. Lithospheric Architecture of the Lhasa Terrane and Its Control on

674 Ore Deposits in the Himalayan-Tibetan Orogen. Economic Geology 110,

675 1541-1575.

676 Hu, X., Garzanti, E., Wang, J., Huang, W., An, W., Webb, A., 2016. The timing of

677 India-Asia collision onset – Facts, theories, controversies. Earth-Science Reviews

678 160, 264-299.

679 Ingersoll, R.V., Bullard, T.F., Ford, R.L., Grimm, J.P., Pickle, J.D., Sares, S.W., 1984.

680 The effect of grain size on detrital modes: a test of the Gazzi-Dickinson

681 point-counting method. Journal of Sedimentary Research 54, 103-116.

682 Kang, Z., Xu, J., Wilde, S.A., Feng, Z., Chen, J., Wang, B., Fu, W., Pan, H., 2014.

683 Geochronology and Geochemistry of the Sangri Group Volcanic Rocks, Southern

684 Lhasa Terrane: Implications for the Early Subduction History of the Neo-Tethys

685 and Gangdese Magmatic Arc. Lithos 200, 157-168.

686 Kapp, P., DeCelles, P.G., Gehrels, G.E., Heizler, M., Ding, L., 2007. Geological records

687 of the Lhasa-Qiangtang and Indo-Asian collisions in the Nima area of central

688 Tibet. Geological Society of America Bulletin 119, 917-933.

689 Kapp, P., Yin, A., Harrison, T.M., Ding, L., 2005. Cretaceous-Tertiary shortening, basin

development, and volcanism in central Tibet. Geological Society of America Bulletin 117, 865-878.

Lai, W., Hu, X., Garzanti, E., Xu, Y., Ma, A., Li, W., 2019. Early Cretaceous sedimentary evolution of the northern Lhasa terrane and the timing of initial Lhasa-Qiangtang collision. Gondwana Research 73, 136-152.

Lang, X., Liu, D., Deng, Y., Tang, J., Wang, X., Yang, Z., Cui, Z., Feng, Y., Yin, Q., Xie, F., Huang, Y., Zhang, J., 2018. Detrital zircon geochronology and geochemistry of Jurassic sandstones in the Xiongcun district, southern Lhasa subterrane, Tibet, China: implications for provenance and tectonic setting. Geological Magazine 156, 683-701.

Lang, X., Tang, J., Li, Z., Huang, Y., Ding, F., Yang, H., Xie, F., Zhang, L., Wang, Q., Zhou, Y., 2014. U–Pb and Re–Os geochronological evidence for the Jurassic porphyry metallogenic event of the Xiongcun district in the Gangdese porphyry copper belt, southern Tibet, PRC. Journal of Asian Earth Sciences 79, 608-622.

Leier, A.L., Decelles, P.G., Kapp, P., Gehrels, G.E., 2007a. Lower Cretaceous Strata in the Lhasa Terrane, Tibet, with Implications for Understanding the Early Tectonic History of the Tibetan Plateau. Journal of Sedimentary Research 77, 809-825.

Leier, A.L., Decelles, P.G., Kapp, P., Lin, D., 2007b. The Takena Formation of the Lhasa terrane, southern Tibet: The record of a Late Cretaceous retroarc foreland basin. Geological Society of America Bulletin 119, 31-48.

Leier, A.L., Paul, K., Gehrels, G.E., Decelles, P.G., 2007c. Detrital zircon

711 geochronology of Carboniferous–Cretaceous strata in the Lhasa terrane, Southern
712 Tibet. Basin Research 19, 361-378.
713 Li, S., Guilmette, C., Yin, C., Ding, L., Zhang, J., Wang, H., Baral, U., 2019. Timing
714 and mechanism of Bangong-Nujiang ophiolite emplacement in the Gerze area of
715 central Tibet. Gondwana Research 71, 179-193.
716 Li, Z., Lippert, P., Ding, L., Song, P., Yue, Y., Van Hinsbergen, D., 2016. Paleomagnetic
717 constraints on the Mesozoic drift of the Lhasa terrane (Tibet) from Gondwana to
718 Eurasia. Geology 44, 737-740.
719 Liu, Y., Gao, S., Hu, Z., Gao, C., Zong, K., Wang, D., 2010a. Continental and oceanic
720 crust recycling-induced melt–peridotite interactions in the Trans-North China
721 Orogen: U–Pb dating, Hf isotopes and trace elements in zircons from mantle
722 xenoliths. Journal of Petrology 51, 537-571.
723 Liu, Y., Hu, Z., Zong, K., Gao, C., Gao, S., Xu, J., Chen, H., 2010b. Reappraisement
724 and refinement of zircon U-Pb isotope and trace element analyses by LA-ICP-MS.
725 Science Bulletin 55, 1535-1546.
726 Liu, Y., Zong, K., Kelemen, P.B., Gao, S., 2008. Geochemistry and magmatic history of
727 eclogites and ultramafic rocks from the Chinese continental scientific drill hole:
728 subduction and ultrahigh-pressure metamorphism of lower crustal cumulates.
729 Chemical Geology 247, 133-153.
730 Liu, Z.C., Ding, L., Zhang, L.Y., Wang, C., Qiu, Z.L., Wang, J.G., Shen, X.L., Deng,
731 X.Q., 2018. Sequence and petrogenesis of the Jurassic volcanic rocks (Yeba

732 Formation) in the Gangdese arc, southern Tibet: Implications for the Neo-Tethyan
733 subduction. Lithos 312-313, 72-88.
734 Ludwig, K.R., 2003. User's manual for Isoplot 3.00: a geochronological toolkit for
735 Microsoft Excel. Berkeley Geochronology Center Special Publication.
736 Ma, Q., Zheng, J., Griffin, W., Zhang, M., Tang, H., Su, Y., Ping, X., 2012. Triassic
737 “adakitic” rocks in an extensional setting (North China): Melts from the cratonic
738 lower crust. Lithos 149, 159-173.
739 McLennan, S.M., Hemming, S., Mcdaniel, D.K., Hanson, G.N., 1993. Geochemical
740 approaches to sedimentation, provenance, and tectonics. Special Paper of the
741 Geological Society of America 284, 21-40.
742 Mo, X., Niu, Y., Dong, G., Zhao, Z., Hou, Z., Zhou, S., Ke, S., 2008. Contribution of
743 syncollisional felsic magmatism to continental crust growth: a case study of the
744 Paleogene Linzizong volcanic succession in southern Tibet. Chemical Geology
745 250, 49-67.
746 Molnar, P., Boos, W.R., Battisti, D.S., 2010. Orographic controls on climate and
747 paleoclimate of Asia: thermal and mechanical roles for the Tibetan Plateau.
748 Annual Review of Earth and Planetary Sciences 38, 77-102.
749 Murphy, M., Yin, A., Harrison, T., Dürr, S., Chen, Z., Ryerson, F., Kidd, W., Wang, X.,
750 Zhou, X., 1997. Did the Indo-Asian collision alone create the Tibetan plateau?
751 Geology 25, 719-722.
752 Nesbitt, H.W., Young, G.M., 1982. Early proterozoic climates and plate motions

753 inferred from major element chemistry of lutites. Nature 299, 715-717.
754 Nesbitt, H.W., Young, G.M., 1996. Petrogenesis of sediments in the absence of
755 chemical weathering: effects of abrasion and sorting on bulk composition and
756 mineralogy. Sedimentology 43, 341-358.
757 Pullen, A., Kapp, P., Gehrels, G.E., DeCelles, P.G., Brown, E.H., Fabijanic, J.M., Ding,
758 L., 2008. Gangdese retroarc thrust belt and foreland basin deposits in the
759 Damxung area, southern Tibet. J. Asian Earth Sci. 33, 323-336.
760 Richter, F.M., Rowley, D.B., Depaolo, D.J., 1992. Sr isotope evolution of seawater: the
761 role of tectonics. Earth and Planetary Science Letters 109, 11-23.
762 Rudnick, R.L., Gao, S., 2003. Composition of the Continental Crust, in: Holland, H.D.,
763 Turekian, K.K. (Eds.), Treatise Geochem. Pergamon, Oxford, pp. 1-64.
764 Sillitoe, R., 1998. Major regional factors favouring large size, high hypogene grade,
765 elevated gold content and supergene oxidation and enrichment of porphyry copper
766 deposits. Porphyry and hydrothermal copper and gold deposits: A global
767 perspective: Adelaide, Australian Mineral Foundation, 21-34.
768 Stern, R.J., 2002. Subduction zones. Reviews of geophysics 40, 3-1-3-38.
769 Sun, G., Hu, X., Sinclair, H., 2017. Early Cretaceous palaeogeographic evolution of the
770 Coqen Basin in the Lhasa Terrane, southern Tibetan Plateau. Palaeogeography,
771 Palaeoclimatology, Palaeoecology 485, 101-118.
772 Sun, G., Hu, X., Xu, Y., BouDagher-Fadel, M.K., 2019. Discovery of Middle Jurassic
773 trench deposits in the Bangong-Nujiang suture zone: Implications for the timing of

774 Lhasa-Qiangtang initial collision. Tectonophysics 750, 344-358.

775 Sun, Z., Pei, J., Li, H., Xu, W., Jiang, W., Zhu, Z., Wang, X., Yang, Z., 2012.
776 Palaeomagnetism of late Cretaceous sediments from southern Tibet: Evidence for
777 the consistent palaeolatitudes of the southern margin of Eurasia prior to the
778 collision with India. Gondwana Research 21, 53-63.

779 Tafti, R., Lang, J.R., Mortensen, J.K., Oliver, J.L., Rebagliati, C.M., 2014. Geology and
780 Geochronology of the Xietongmen (Xiongcun) Cu-Au Porphyry District,
781 Southern Tibet, China. Economic Geology 109, 1967-2001.

782 Tafti, R., Mortensen, J.K., Lang, J.R., Rebagliati, M., Oliver, J.L., 2009. Jurassic U-Pb
783 and Re-Os ages for the newly discovered xietongmen Cu-Au porphyry district,
784 tibet, PRC: Implications for metallogenic epochs in the Southern gangdese belt.
785 Economic Geology 104, 127-136.

786 Taylor, S.R., McLennan, S.M., 1985. The continental crust: its composition and
787 evolution. Blackwell's, Oxford.

788 Vermeesch, P., 2012. On the visualisation of detrital age distributions. Chemical
789 Geology 312-313, 190-194.

790 Wang, C., Ding, L., Zhang, L.Y., Kapp, P., Pullen, A., Yue, Y.H., 2016. Petrogenesis of
791 Middle–Late Triassic volcanic rocks from the Gangdese belt, southern Lhasa
792 terrane: Implications for early subduction of Neo-Tethyan oceanic lithosphere.
793 Lithos 262, 320-333.

794 Wang, C., Li, X., Liu, Z., Li, Y., Jansa, L., Dai, J., Wei, Y., 2012. Revision of the

795 Cretaceous–Paleogene stratigraphic framework, facies architecture and
796 provenance of the Xigaze forearc basin along the Yarlung Zangbo suture zone.
797 Gondwana Research 22, 415-433.
798 Wang, J.-G., Hu, X., Garzanti, E., An, W., Liu, X.-C., 2017a. The birth of the Xigaze
799 forearc basin in southern Tibet. Earth and Planetary Science Letters 465, 38-47.
800 Wang, J.-G., Hu, X., Garzanti, E., Ji, W.-Q., Liu, Z.-C., Liu, X.-C., Wu, F.-Y., 2017b.
801 Early Cretaceous topographic growth of the Lhasaplano, Tibetan Plateau:
802 Constraints from the Damxung Conglomerate: Topographic growth on Tibetan
803 Plateau. Journal of Geophysical Research Solid Earth 122.
804 Wei, Y., Zhao, Z., Niu, Y., Zhu, D.C., Dong, L., Wang, Q., Hou, Z., Mo, X., Wei, J.,
805 2017. Geochronology and geochemistry of the Early Jurassic Yeba Formation
806 volcanic rocks in southern Tibet: Initiation of back-arc rifting and crustal accretion
807 in the southern Lhasa Terrane. Lithos s278–281, 477-490.
808 Wronkiewicz, D.J., Condie, K.C., 1987. Geochemistry of Archean shales from the
809 Witwatersrand Supergroup, South Africa: Source-area weathering and provenance.
810 *Geochim. Cosmochim. Acta* 51, 2401-2416.
811 Wu, F.-Y., Ji, W.-Q., Liu, C.-Z., Chung, S.-L., 2010. Detrital zircon U–Pb and Hf
812 isotopic data from the Xigaze fore-arc basin: constraints on Transhimalayan
813 magmatic evolution in southern Tibet. Chemical Geology 271, 13-25.
814 Wu, F.-Y., Yang, Y.-H., Xie, L.-W., Yang, J.-H., Xu, P., 2006. Hf isotopic compositions
815 of the standard zircons and baddeleyites used in U–Pb geochronology. Chemical

816 Geology 234, 105-126.

817 Yan, D., Chen, D., Wang, Q., Wang, J., 2010. Large-scale climatic fluctuations in the
818 latest Ordovician on the Yangtze block, south China. Geology 38, 599-602.

819 Yin, A., Harrison, T.M., 2000. Geologic evolution of the Himalayan-Tibetan orogen.
820 Annual Review of Earth and Planetary Sciences 28, 211-280.

821 Zhang, K.J., Zhang, Y.X., Tang, X.C., Xia, B., 2012. Late Mesozoic tectonic evolution
822 and growth of the Tibetan plateau prior to the Indo-Asian collision. Earth-Science
823 Reviews 114, 236-249.

824 Zhang, Q., Ding, L., Cai, F., Xu, X.-X., Zhang, L., Xu, Q., Willems, H., 2011. Early
825 Cretaceous Gangdese retroarc foreland basin evolution in the Selin Co basin,
826 central Tibet: Evidence from sedimentology and detrital zircon geochronology.
827 Geological Society, London, Special Publications 353, 27-44.

828 Zhang, Z., Zhao, G., Santosh, M., Wang, J., Dong, X., Shen, K., 2010. Late Cretaceous
829 charnockite with adakitic affinities from the Gangdese batholith, southeastern
830 Tibet: Evidence for Neo-Tethyan mid-ocean ridge subduction? Gondwana
831 Research 17, 615-631.

832 Zhu, D.-C., Pan, G.-T., Chung, S.-L., Liao, Z.-L., Wang, L.-Q., Li, G.-M., 2008.
833 SHRIMP zircon age and geochemical constraints on the origin of Lower Jurassic
834 volcanic rocks from the Yeba Formation, southern Gangdese, South Tibet.
835 International Geological Review 50, 442-471.

836 Zhu, D.-C., Zhao, Z.-D., Niu, Y., Dilek, Y., Hou, Z.-Q., Mo, X.-X., 2013. The origin

and pre-Cenozoic evolution of the Tibetan Plateau. Gondwana Research 23, 1429-1454.

Zhu, D.-C., Zhao, Z.-D., Niu, Y., Mo, X.-X., Chung, S.-L., Hou, Z.-Q., Wang, L.-Q., Wu, F.-Y., 2011a. The Lhasa Terrane: Record of a microcontinent and its histories of drift and growth. Earth and Planetary Science Letters 301, 241-255.

Zhu, D.C., Li, S.M., Cawood, P.A., Wang, Q., Zhao, Z.D., Liu, S.A., Wang, L.Q., 2016. Assembly of the Lhasa and Qiangtang terranes in central Tibet by divergent double subduction. Lithos 245, 7-17.

Zhu, D.C., Wang, Q., Cawood, P.A., Zhao, Z.D., Mo, X.X., 2017. Raising the Gangdese Mountains in southern Tibet. Journal of Geophysical Research: Solid Earth 122.

Zhu, D.C., Zhao, Z.D., Niu, Y., Dilek, Y., Mo, X.X., 2011b. Lhasa terrane in southern Tibet came from Australia. Geology 39, 727-730.

850 **Figure Captions**

851 **Fig. 1** (A) Schematic tectonic framework of the Tibetan Plateau (modified after Wu et
852 al., 2010) and (B) simplified geological map showing sample locations.

853

854 **Fig. 2** Outcrops show (A) mudstone interbedded with fine-grained sandstone in the
855 Chumulong Formation; (B) red beds of the Shexing Formation and (C) alternating
856 beds of sandstone and shale in the Ngamring Formation. Microphotographs show: (D)
857 the Chumulong Formation mudstone (D47D), (E) Shexing Formation sandstone
858 (MX1105) and (F) Ngamring Formation sandstone (RK1602). Q, quartz; Pl,
859 plagioclase; Kfs, potassic feldspar; Lv, volcanic lithic fragment; Ls, sedimentary lithic
860 fragment.

861

862 **Fig. 3** The Q-F-L ternary plot (Dickinson, 1985) showing clastic composition of
863 samples from the Yeba, Xiongcun, Chumulong and Shexing Formations. The
864 Xiongcun Formation data are from Lang et al., (2018). Q, quartz; F, feldspars; L,
865 lithic fragments; RO, recycled orogen; UMA, undissected magmatic arc; TMA,
866 transitional magmatic arc; DMA, dissected magmatic arc; BU, basement uplift; TC,
867 transitional continental; CI, craton interior.

868

869 **Fig. 4** Kernel density estimation plots of detrital zircon U-Pb ages for clastic rocks

from the Yeba (A and B), Chumulong (C and D) and Shexing (E and F) Formations

Fig. 5 Hf isotope composition of detrital zircons from the Chumulong and Shexing Formations. The field of GMA and Lhasa basement are constructed based on the dataset in Hou et al., (2015) and references therein. Data of the Duoni Formation from Sun et al., (2017). GMA, Gangdese magmatic arc; DM, depleted mantle; CHUR, chondritic uniform reservoir.

Fig. 6 (A-F) Plot of SiO_2 vs. abundances of major element oxide for the sandstone and mudstone samples; (G-L) plots of modal volcanic lithics proportion vs. concentrations or ratios of selected elements for the sandstone samples.

Fig. 7 (A-D) Chondrite-normalized REE and (E) UCC-normalized multielement diagrams for the sediments in the southern Lhasa terrane. Chondrite and UCC (upper continental crust) data from Sun and McDonough (1989) and Rudnick and Gao (2003), respectively. Unweathered Yeba volcanics data from Wei et al. (2017).

Fig. 8 Ternary plots of (A) A-CN-K and (B) A-CNK-FM showing sandstones and mudstones from the Jurassic-Cretaceous strata in the southern Lhasa terrane (after Nesbitt and Young, 1989; McLennan et al., 1993). The Xiongcun Formation data are from Lang et al., (2018). A = Al_2O_3, C = CaO*, N = Na_2O, K = K_2O, F = total Fe as

FeO, M = MgO.

Fig. 9 Plot of Th vs. Th/U for the clastic rocks from the southern Lhasa terrane (after McLennan et al., 1993). Yeba Formation volcanic rock data from Wei et al. (2017) and Zhu et al. (2008).

Fig. 10 Ternary plots of Th-Sc-Zr/10 and La-Th-Sc for the sediments from the southern Lhasa terrane, where GMA = Gangdese magmatic arc, ACM = active continental margin, PCM = passive continental margin, CA = continental arcs, OA = oceanic arcs (After Bhatia and Crook, 1986). GMA Array is defined using data of the Yeba volcanic rocks (Wei et al., 2017).

Fig. 11 Binary diagram of La/Sc-Co/Th showing two-component mixing trend. Mafic endmember is represented by the Yeba Formation basalt (sample YB1307 in Wei et al., 2017) with Co=39.3ppm, Th=1.18ppm, La=10.9ppm and Sc=33.8ppm. Silicic endmember is represented by the Yeba Formation rhyolite (sample YB1318 in Wei et al., 2017) with Co=3.1ppm, Th=8.89ppm, La=27.3ppm and Sc=6.4ppm.

Fig. 12 Stratigraphic columns showing compositional variations of the sediments and detrital zircon sample location in different lithostratigraphic units. Columns after An et al. (2014); Leier et al. (2007a); Leier et al. (2007b); Wang et al. (2012); Zhu et al.

912 (2013). CIA serves as an indicator of chemical weathering intensity. Eu/Eu* reflects
913 enrichment of volcanic lithics. Na_2O/K_2O measures compositional maturity.
914 Thicknesses of different units are not to scale. Timescale in Ma from Cohen et al.
915 (2013). The average composition of upper continental crust (Eu/Eu*=0.65,
916 Na_2O/K_2O=1.2) are introduced for reference.
917
918 **Fig.13** Summary of detrital zircon age spectra of sedimentary rocks of this study and
919 previous work. Important age peaks are shown in colored bands. The red line
920 represents kernel density estimation. Data of the (A) western Australia, (B)
921 Permo-Carboniferous Lhasa and (G) western Qiangtang from Zhu et al., 2011b and
922 references therein; (C) Late Triassic Lhasa from Cai et al. (2016); (D) Early Jurassic
923 Lhasa from this study; (E) Early Cretaceous Lhasa from Leier et al. (2007c) and this
924 study; (F) Late Cretaceous Lhasa from Kapp et al. (2007), Leier et al. (2007c), Pullen
925 et al. (2008) and this study.
926
927 **Fig. 14** Schematic illustrations showing tectonic evolution of the Lhasa terrane during
928 the Jurassic-Cretaceous time (not to scale). See text for details.
929
930 **Table Caption**
931 **Table 1** Summarized characteristics of detrital zircon U-Pb ages for clastic samples

932 from the southern Lhasa terrane

Table 1 Summarized characteristics of detrital zircon U-Pb ages for samples from southern Lhasa terrane

Formation	Sample	Number of analyses	Maximum depositional age (Ma)	YSG[a] (Ma, 1σ)	YC1σ(2+)[a] (Ma)	YC2σ(3+)[a] (Ma)	Percentage of Mesozoic ages	Mesozoic zircons with εHf(t)>0
Yeba	D54	104	179[b]	179±2	563.5±3.6 (n=6)	248.0±3.5 (n=3)	4.8% (5 out of 104)	
Chumulong	D47A	103	121	117±1	121.1±1.1 (n=4)	121.1±1.1 (n=4)	24% (25 out of 103)	41% (18 out of 44)
	D47B	109	122	105±1	122.4±1.3 (n=4)	123.3±0.9 (n=7)	34% (37 out of 109)	
	D47C	68	119[b]	119±2	394.0±4.2 (n=4)	401.4±2.2 (n=11)	1.4% (1 out of 68)	
	D47E	47	109[b]	109±1	231.5±2.8 (n=2)	247.9±2.6 (n=3)	32% (15 out of 47)	
Shexing	MX1102	113	88	84±2	88.5±1.4 (n=2)	88.8±1.3 (n=3)	25% (28 out of 113)	67% (70 out of 104)
	MX1104	90	90	85±1	89.9±0.7 (n=15)	89.7±0.6 (n=18)	52% (47 out of 90)	
	MX1106	86	88	82±2	87.7±0.5 (n=30)	87.1±0.5 (n=35)	83% (71 out of 86)	
	MX1108	88	91[b]	91±2	213.3±3.5 (n=3)	213.3±3.5 (n=3)	6.8% (6 out of 88)	

[a] Youngest detrital zircon age measurement after Dickinson and Gehrels (2009). YSG, youngest single detrital zircon age; YC1σ(2+), weighted mean age of two or more youngest grains that overlap in age at 1σ; YC2σ(3+), weighted mean age of three or more youngest grains that overlap in age at 2σ.

[b] YSG is suggested due to the inconsistency of YC2σ with the depositional ages determined via other samples/methods.

Wei et al. Fig.1 W179mm - H163mm (2-column fitting image)

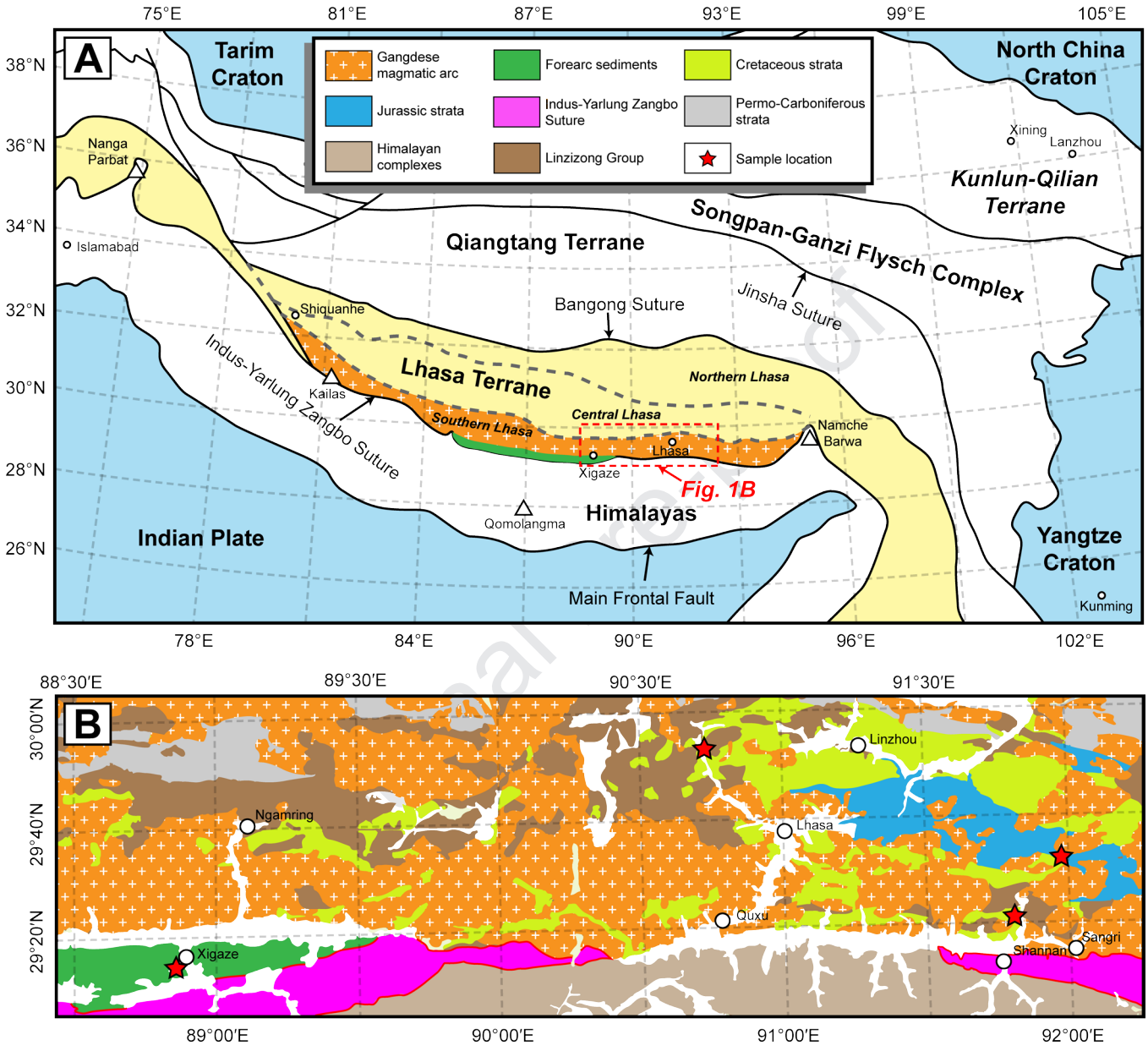

Wei et al. Fig.2 W132mm - H149mm (2-column fitting image)

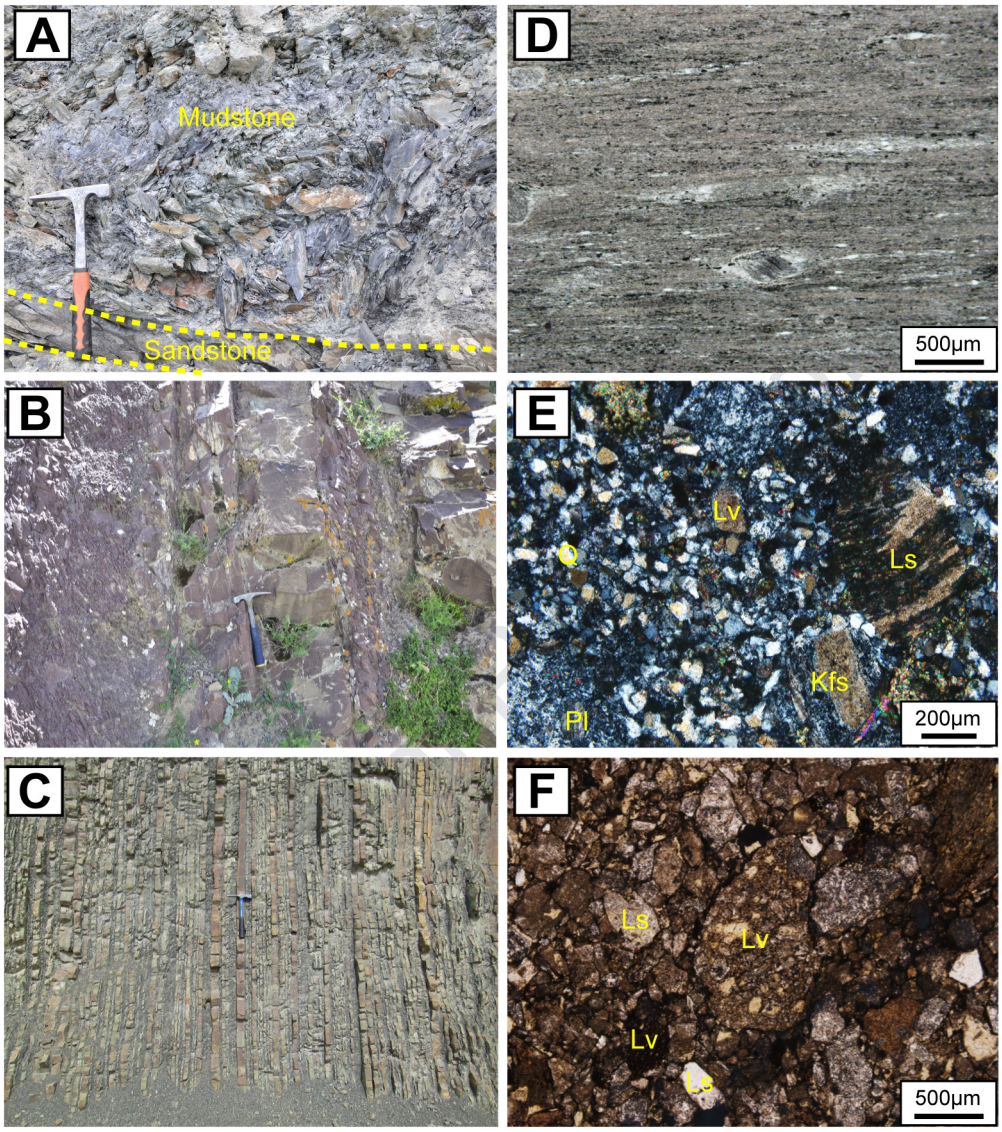

Wei et al. Fig.3 W77mm - H75mm (1-column fitting image)

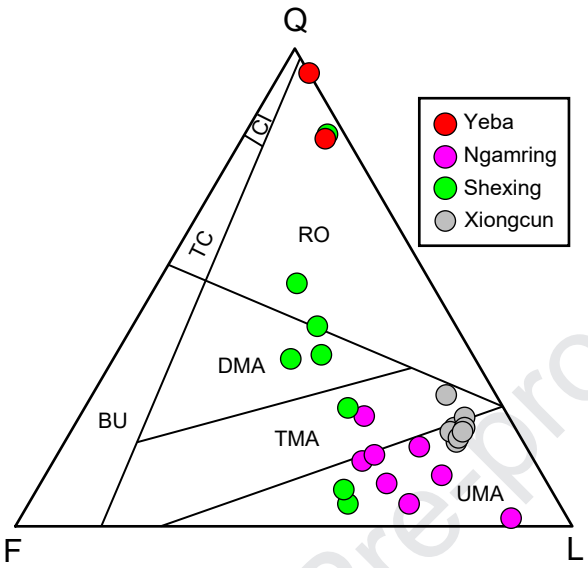

Wei et al. Fig.4 W174mm - H151mm (2-column fitting image)

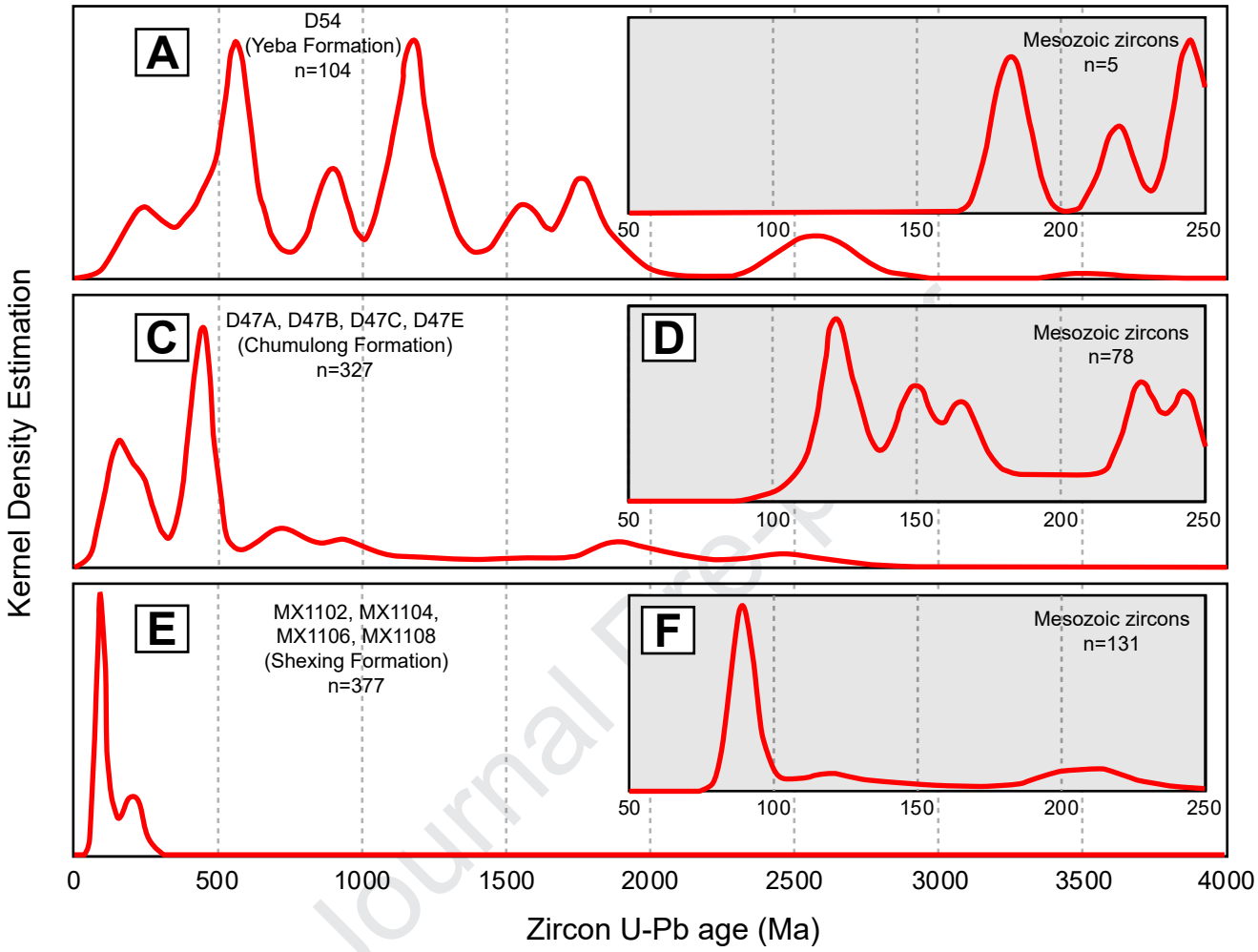

Wei et al. Fig.5 W90mm - H69mm (1-column fitting image)

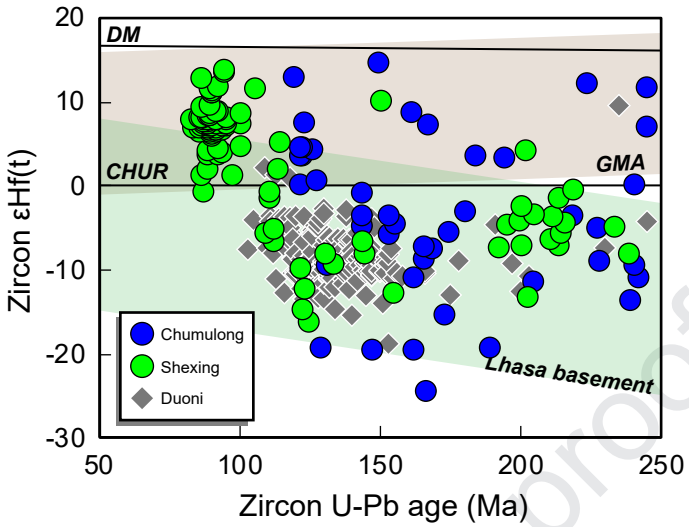

Wei et al. Fig.6 W179mm - H188mm (2-column fitting image)

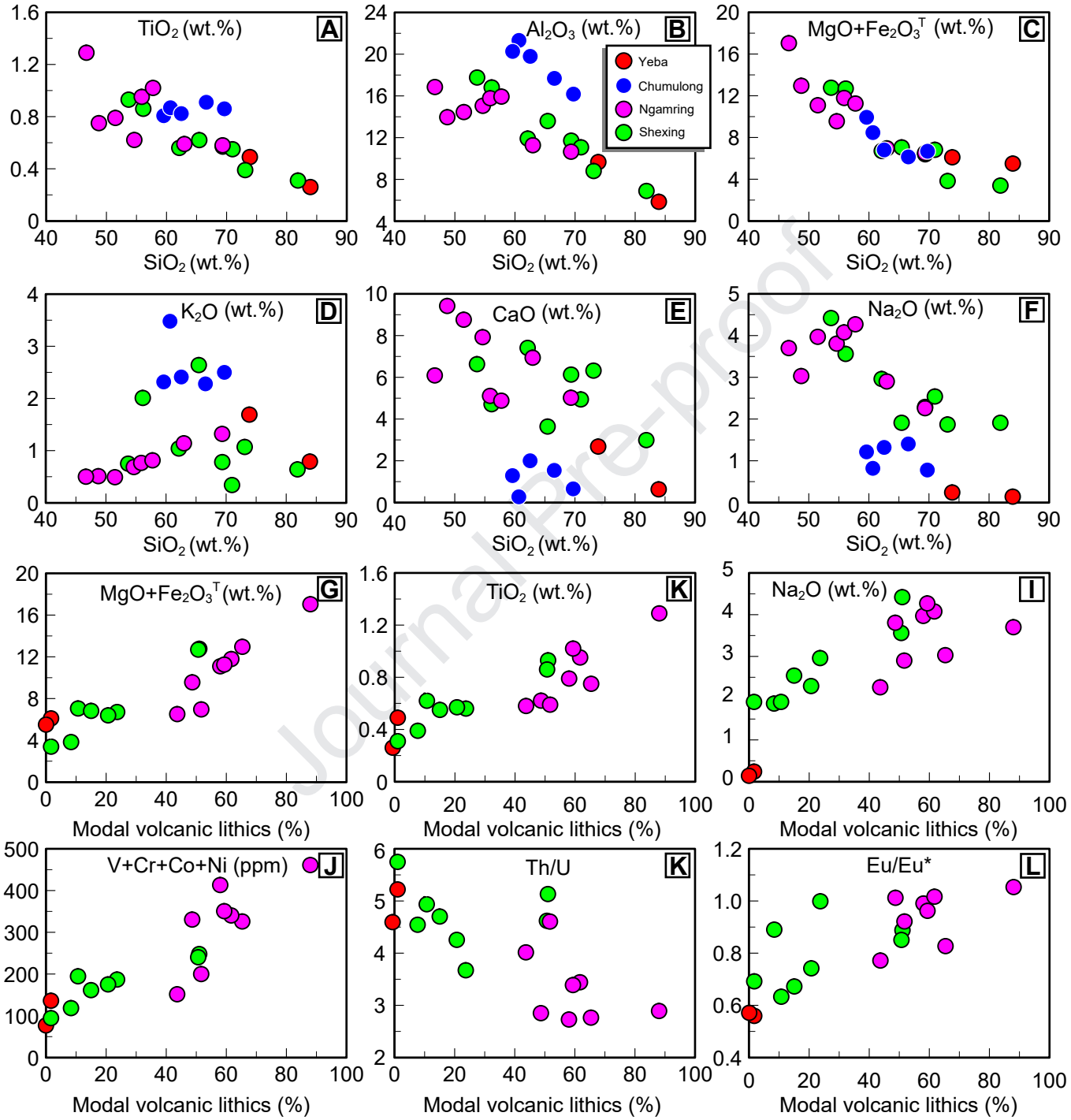

Wei et al. Fig.7 W158mm - H179mm (2-column fitting image)

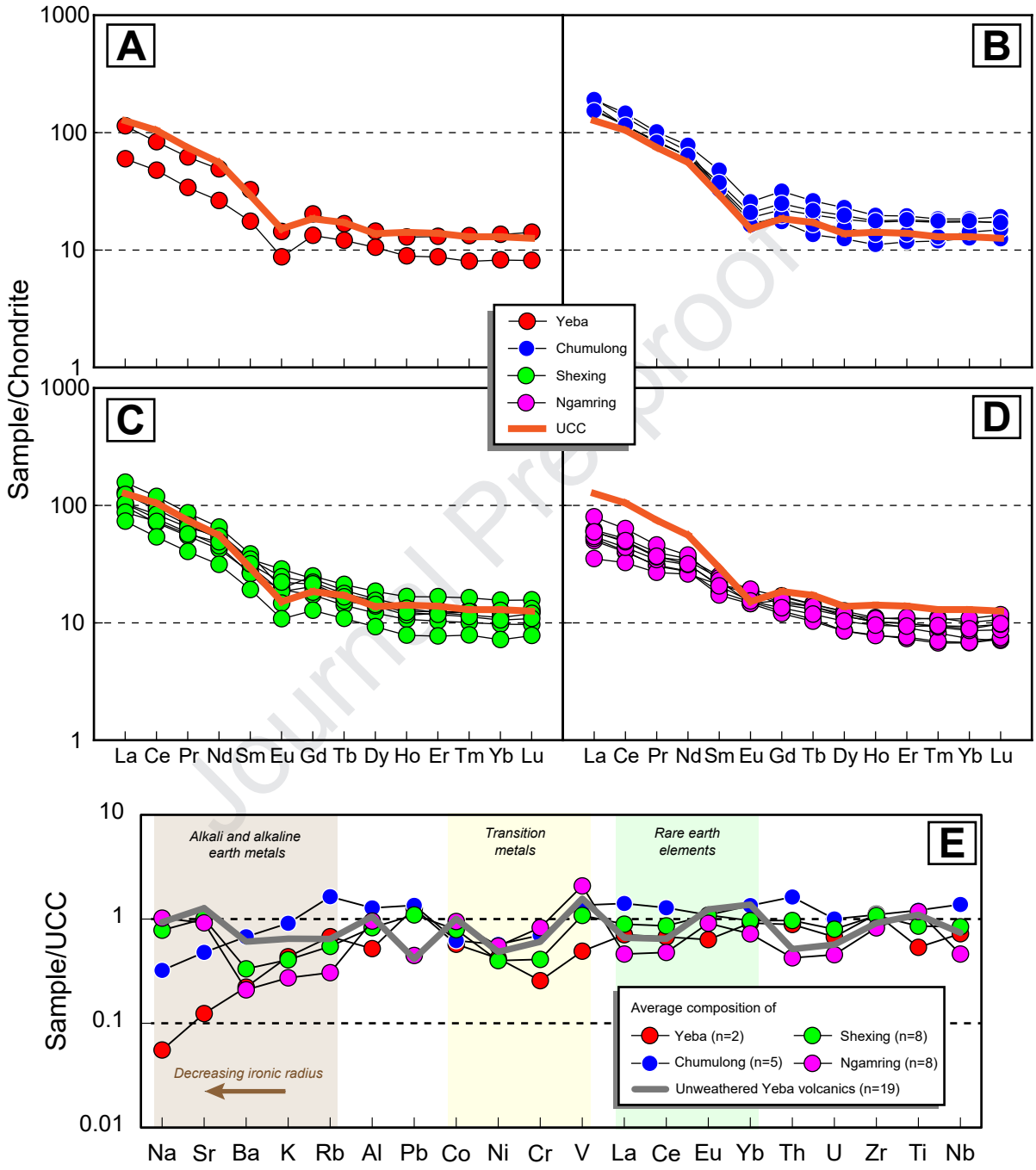

Wei et al. Fig.8 W170mm - H74mm (2-column fitting image)

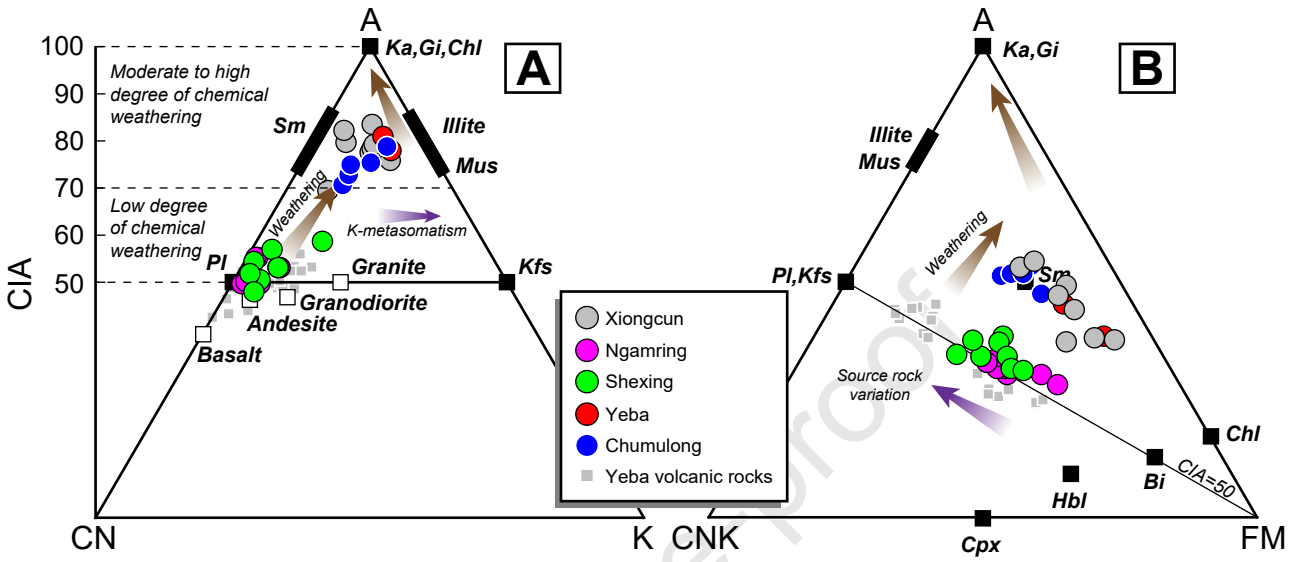

Wei et al. Fig.9 W77mm - H60mm (1-column fitting image)

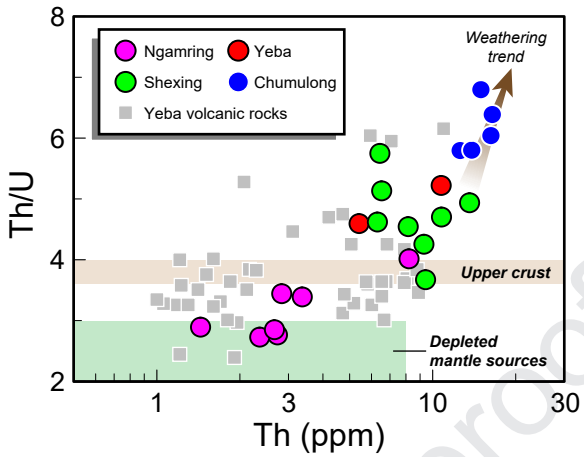

Wei et al. Fig.10 W168mm - H76mm (2-column fitting image)

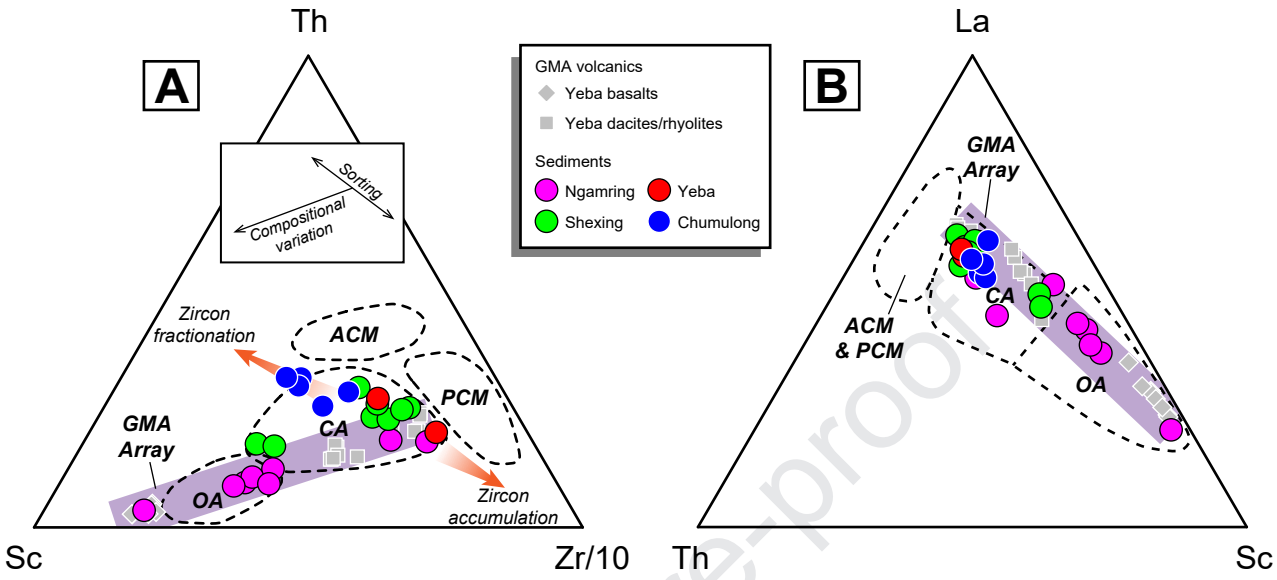

Wei et al. Fig.11 W78mm - H59mm (1-column fitting image)

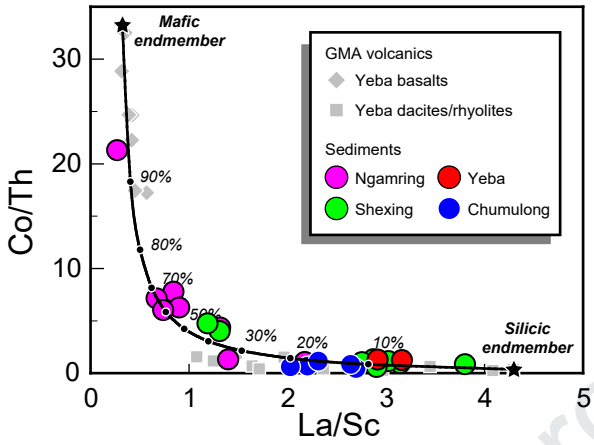

Wei et al. Fig.12 W150mm - H143mm (2-column fitting image)

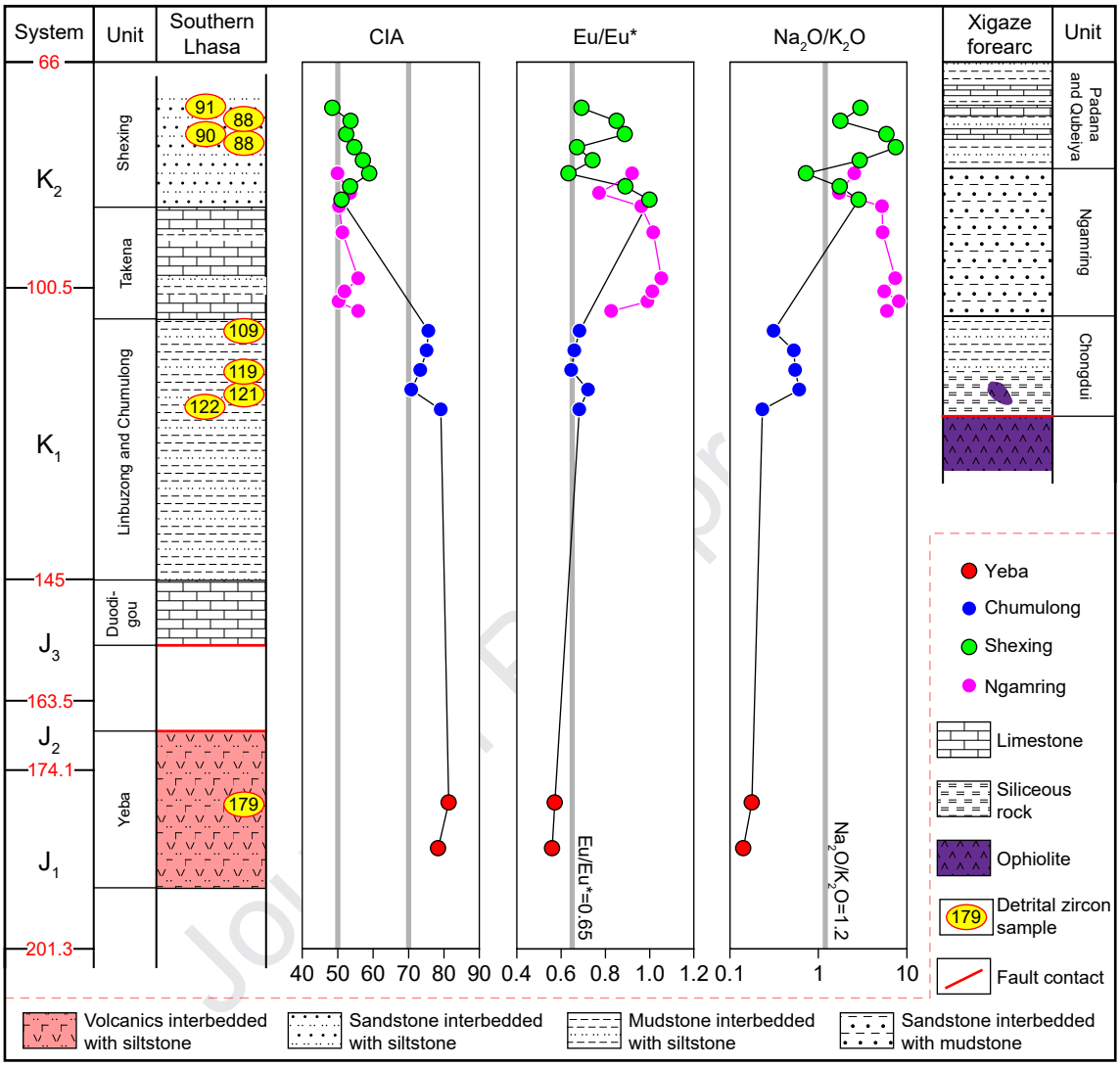

Wei et al. Fig.13 W156mm - H174mm (2-column fitting image)

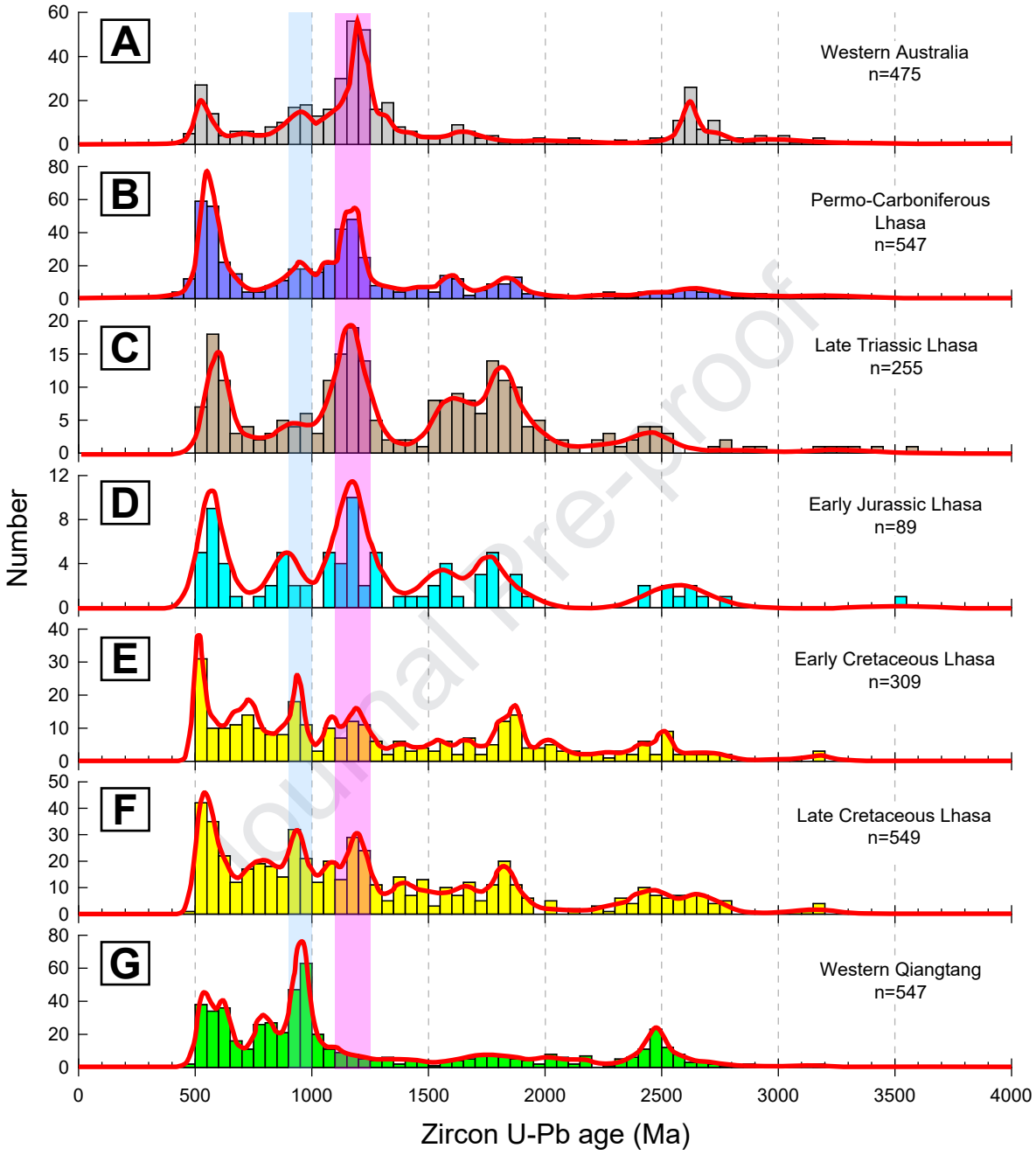

Wei et al. Fig.14 W121mm - H223mm (2-column fitting image)

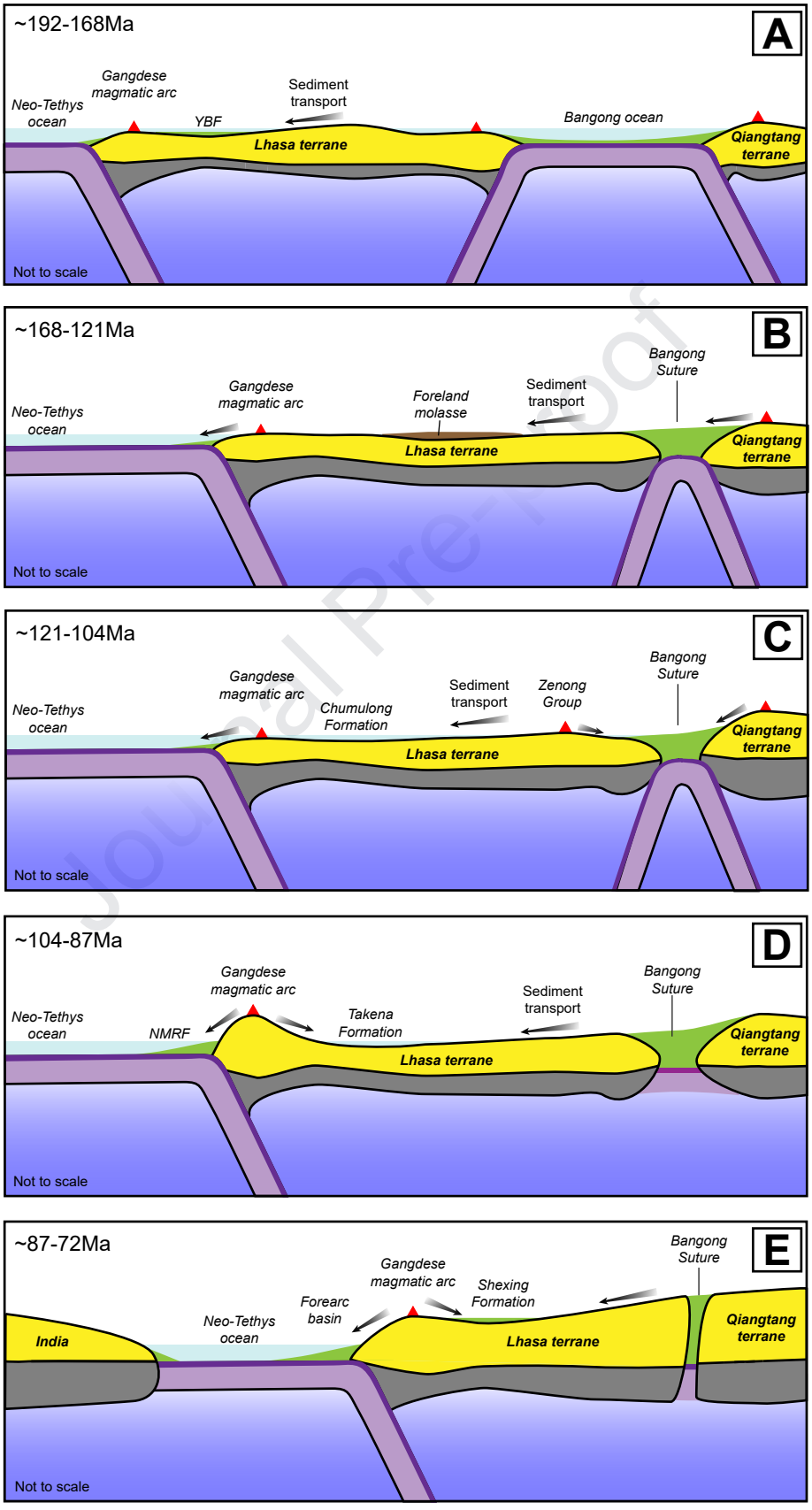

Highlights

- Jurassic-Cretaceous tectonic evolution of the Lhasa terrane was reconstructed.
- Maximum depositional ages of strata in the southern Lhasa terrane were constrained.
- Sedimentary processes were quantified using sedimentary geochemistry approach.
- Two-component mixing model was constructed to evaluate the sedimentary provenances.
- The Lhasa terrane received clasts from Qiangtang since the Early Cretaceous.